The Journal of Chemical Physics ARTICLE scitation.org/journal/jcp

Accuracy of approximate methods for the calculation of absorption-type linear spectra with a complex system–bath coupling

Cite as: J. Chem. Phys. 157, 095103 (2022); doi: 10.1063/5.0100977
Submitted: 27 May 2022 • Accepted: 9 August 2022 •
Published Online: 7 September 2022

J. A. Nöthling,[1,2] Tomáš Mančal,[3] and T. P. J. Krüger[1,2,a)]

AFFILIATIONS

[1] Department of Physics, University of Pretoria, 0002 Pretoria, South Africa
[2] National Institute for Theoretical and Computational Sciences (NITheCS), Stellenbosch, South Africa
[3] Faculty of Mathematics and Physics, Charles University, Ke Karlovu 5, CZ-12116 Prague 2, Czech Republic

[a)] **Author to whom correspondence should be addressed:** tjaart.kruger@up.ac.za

ABSTRACT

The accuracy of approximate methods for calculating linear optical spectra depends on many variables. In this study, we fix most of these parameters to typical values found in photosynthetic light-harvesting complexes of plants and determine the accuracy of approximate spectra with respect to exact calculation as a function of the energy gap and interpigment coupling in a pigment dimer. We use a spectral density with the first eight intramolecular modes of chlorophyll *a* and include inhomogeneous disorder for the calculation of spectra. We compare the accuracy of absorption, linear dichroism, and circular dichroism spectra calculated using the Full Cumulant Expansion (FCE), coherent time-dependent Redfield (ctR), and time-independent Redfield and modified Redfield methods. As a reference, we use spectra calculated with the exact stochastic path integral evaluation method. We find the FCE method to be the most accurate for the calculation of all spectra. The ctR method performs well for the qualitative calculation of absorption and linear dichroism spectra when the pigments are moderately coupled (~15 cm^{-1}), but ctR spectra may differ significantly from exact spectra when strong interpigment coupling (>100 cm^{-1}) is present. The dependence of the quality of Redfield and modified Redfield spectra on molecular parameters is similar, and these methods almost always perform worse than ctR, especially when the interpigment coupling is strong or the excitonic energy gap is small (for a given coupling). The accuracy of approximate spectra is not affected by resonance with intramolecular modes for typical system–bath coupling and disorder values found in plant light-harvesting complexes.

I. INTRODUCTION

Linear optical spectroscopy is a crucial analytical tool in biology, chemistry, materials science, molecular physics, and various other disciplines. It provides information about, e.g., the dipole strengths and orientations,[1–3] energy landscape,[4–7] exciton structure,[8,9] and stoichiometry[10] in pigment aggregates. In principle, all the information contained in an experimental spectrum could be extracted by comparison with exact simulations. The exact calculation of linear spectra is possible for Gaussian environmental fluctuations,[11] but is computationally expensive, and is generally only performed in order to benchmark approximate calculations on simple systems. One reliable approach for the calculation of exact spectra is the Hierarchical Equations of Motion (HEOM) method,[11,12] which requires solving many tiers of equations for the system's reduced density matrix and is therefore memory intensive.[13] The addition of a single high-frequency mode to the environment's spectral density greatly increases the number of equations that have to be solved.[14] An alternative approach is the method of Exact Stochastic Path Integral Evaluation (PI), which is easier to implement than HEOM, converges faster, and is not memory intensive.[15] Nevertheless, as we discuss in this article, this method also scales poorly with the number of high-frequency modes.

The intractability of exact methods prevents their use for the calculation of ensemble spectra of large, disordered aggregates with complex system–environment coupling. Many different approaches to the approximate calculation of linear optical spectra exist.[16–19] Most of these methods rely on the second-order cumulant

expansion of the system–environment coupling, and they differ mainly in their treatment of the off-diagonal elements of this coupling in the exciton basis. In two common and economical approaches, the time-independent Redfield and modified Redfield rates are included phenomenologically in the calculation of linear spectra to account for the lifetime broadening of electronic transitions.[6,19,20] A more explicit treatment of the second-order cumulant expansion brings about the Full Cumulant Expansion (FCE) method,[18,21] for which the time-dependent expressions are slower to evaluate than the rates of the Redfield-type methods, but are more accurate. The application of the secular approximation to FCE yields the faster, but less accurate, coherent time-dependent Redfield (ctR) method.[19]

When calculating approximate spectra, it is essential to know what level of accuracy to expect from the method that is used, under which conditions it may be substituted with a more cost-efficient one, and what effect different approximations have on the quality of spectra. Since the approximate methods discussed above are used frequently, rely on different, common, approximations, and vary significantly in speed, their comparison provides valuable insight into the capabilities and limitations of approximate methods, in general, and how they may be improved. Although some of these approximate methods have been compared with one another, the previous comparisons were either done for a specific system without much variation in parameters[21] or for model systems with unrealistic system–environment coupling.[19,22] Therefore, there is clearly a need for a systematic comparison of approximate methods for calculating linear spectra in a system with realistic system–environment coupling.

Gelzinis *et al.*[19] compared the accuracy of absorption spectra obtained for a dimer using the ctR, Redfield, and modified Redfield methods. They calculated the spectral qualities as functions of various system and environment parameters that they varied one at a time. Inhomogeneous disorder, for instance, was considered as one of their parameters, but was set to zero when other parameters were varied. They found ctR spectra to agree significantly better with exact spectra over a wide range of parameter values than spectra calculated with the Redfield and modified Redfield methods. They also found the modified Redfield method to perform worst for all the parameter values that they considered. For most of their calculations, Gelzinis *et al.* used an overdamped Brownian oscillator spectral density without any underdamped (high-frequency) modes. They included a single high-frequency mode for one of their comparison calculations and treated its energy as the only variable in that comparison.

Cupellini *et al.*[21] used the FCE and modified Redfield methods to calculate absorption and circular dichroism (CD) spectra of the purple bacterial light-harvesting complex LH2 and compared these spectra to experimental data. The FCE spectra agreed better with experimental spectra than the modified Redfield spectra did. However, because of the uncertainty about the true molecular parameters, none of the spectra agreed well with the experimental spectra, and their comparison is consequently not as conclusive as it would be for a model study.

In real pigment aggregates, many of the parameters considered by Gelzinis *et al.*, such as the amplitude and shape of the environmental spectral density and the variance of the inhomogeneous disorder, can be estimated accurately and have similar values for a wide range of aggregates. The parameters that typically have the largest variation in the simulation of spectra are the temperature, energies of pigments, and interpigment couplings.

To our knowledge, neither FCE nor ctR has been used for the calculation of linear dichroism (LD) spectra, and the non-secular dipole dependence of LD has not been previously derived. In this article, we compare absorption, LD, and CD spectra calculated with the FCE, ctR, standard Redfield, and modified Redfield methods. We determine the dependence of the spectral accuracy on the simultaneous variation of pigment energy and interpigment coupling at two different temperatures for inhomogeneously broadened absorption-type spectra. Unlike Gelzinis *et al.*,[19] who used HEOM for their exact calculations, we calculate exact spectra using the more economical PI method.[15] This allows us to better model environmental interactions by including eight high-frequency modes in our spectral density. In order for our conclusions to be accurate for photosynthetic light-harvesting complexes, we use the parameters of the first eight intramolecular modes of chlorophyll *a*. The inclusion of several high-frequency modes allows us to determine the effect of excitonic energy gap resonance with intramolecular modes on the quality of calculated linear spectra.

II. THEORY

A. Hamiltonian

The spectroscopic response from a light-harvesting complex originates from quantum dynamics that are governed by the Hamiltonian

$$\hat{H} = \hat{H}_{\mathrm{mol}} + \hat{H}_{\mathrm{rad-mat}}(t), \tag{1}$$

in which $\hat{H}_{\mathrm{rad-mat}}(t)$ describes the light–matter interaction in the semi-classical approximation (hence the time-dependence of the Hamiltonian) and $\hat{H}_{\mathrm{mol}}$ describes the influence of molecular attributes on the dynamics.

We treat the pigment aggregate as an open quantum system and partition $\hat{H}_{\mathrm{mol}}$ into a system, bath, and system–bath interaction part,

$$\hat{H}_{\mathrm{mol}} = \hat{H}_{\mathrm{S}} + \hat{H}_{\mathrm{B}} + \hat{H}_{\mathrm{SB}}. \tag{2}$$

For a molecular system composed of multiple interacting molecules with optical bandgaps, the electronic ground state is the collective electronic state in which all molecules are found in their respective electronic ground states. Optical properties of the system are characterized by transitions to the so-called *single exciton* band, which is composed of collective electronic states with an excitation residing on a single molecule of the system. For a light-harvesting complex with N pigment molecules, the ground state $|g\rangle$ can thus be represented by the direct product of molecular ground states $|g\rangle = \prod_{n=1}^{N} |g_n\rangle$, where $|g_n\rangle$ is the ground state of pigment n. There are N collective singly excited states represented by $|n\rangle = \prod_{\substack{m=1 \\ m\neq n}}^{N} |g_m\rangle|\epsilon_n\rangle$, where $|\epsilon_n\rangle$ denotes the electronically excited state of pigment n. The system Hamiltonian, the so-called Frenkel exciton Hamiltonian, involves the energies ε_n of these collective states and their mutual interaction energies J_{mn}. It has the general form

$$\hat{H}_S = \sum_{n=1}^{N} \varepsilon_n |n\rangle\langle n| + \sum_{n=1}^{N} \sum_{\substack{m=1 \\ m\neq n}}^{N} J_{mn} |m\rangle\langle n|, \tag{3}$$

where the ground-state energy is set to zero and ε_n is the energy of the vertical (Franck–Condon) transition on pigment n.

Electronic transitions observed by spectroscopic means occur between the ground state and excited eigenstates of the Hamiltonian in Eq. (3). These eigenstates can be found by performing an affine *exciton* transformation on $\hat{H}_S$, which renders it in the simple form

$$\hat{H}_S = \sum_{\alpha=1}^{N} \varepsilon_\alpha |\alpha\rangle\langle\alpha|, \tag{4}$$

where the exciton states are linear combinations of the site excitations, i.e., $|\alpha\rangle = \sum_{n=1}^{N} c^{n\alpha}|n\rangle$, and ε_α represent the eigenenergies of the Hamiltonian.

The exciton energies are modulated by nuclear fluctuations in the pigment molecules and their environment and are therefore coupled to phonon modes of the environment and intramolecular vibrational modes. These modes together constitute the *bath* and are modeled as an infinite set of independent harmonic oscillators,

$$\hat{H}_B = \sum_{k=1}^{\infty} \frac{\omega_k}{2} (\hat{\boldsymbol{p}}_k^2 + \hat{\boldsymbol{q}}_k^2) \otimes \hat{I}_S, \tag{5}$$

where $\hat{I}_S$ is the identity operator in the system's Hilbert space, and ω_k, $\hat{\boldsymbol{p}}_k$, and $\hat{\boldsymbol{q}}_k$ are the frequency and position and momentum operators of the kth mode, respectively. In this article, we use units such that $\hbar = 1$. Typically, the system–bath coupling is assumed to be linear,

$$\hat{H}_{SB} = -\sum_{k=1}^{\infty} \sum_{n=1}^{N} \omega_k d_{k,nn} \hat{q}_k |n\rangle\langle n|, \tag{6}$$

and its strength is characterized by the reorganization energy

$$\lambda_n = \sum_{k=1}^{\infty} \frac{\omega_k}{2} d_{k,nn}^2 \tag{7}$$

associated with each electronic transition. The reorganization energy can often be estimated from experimental measurements (e.g., from the Stokes shift) and depends on the dimensionless shift $d_{k,nn}$ of the excited state harmonic potential energy surface with respect to the ground state potential energy surface. In Eq. (6), spatial dimensions were separated so that $\hat{q}_k$ is a scalar operator.

The light–matter interaction is treated through linear coupling to a classical electric field $\boldsymbol{E}(t)$,

$$\hat{H}_{\text{rad-mat}}(t) = -\hat{\boldsymbol{\mu}} \cdot \boldsymbol{E}(t), \tag{8}$$

with the transition dipole moment operator given by

$$\hat{\boldsymbol{\mu}} = \sum_{n=1}^{N} \boldsymbol{\mu}_n (|n\rangle\langle g| + |g\rangle\langle n|), \tag{9}$$

where the vector $\boldsymbol{\mu}_n$ is the transition dipole moment of the transition from the ground to the excited state on the nth molecule. The dipole moments are assumed to be independent of the nuclear coordinates (i.e., the Condon approximation is made).

B. Linear spectra

During linear spectroscopic measurements, the incident electromagnetic field induces a transverse molecular polarization, which generates an additional electric field interfering with the incident fields. The combination of these fields is then measured as a field leaving the macroscopic molecular sample. The linear response (first-order perturbation of the system) is characterized by the dipole–dipole correlation function

$$\langle \mu(t)\mu(0)\rangle = \text{Tr}[e^{i\hat{H}_{\text{mol}}t} \hat{\boldsymbol{\mu}} e^{-i\hat{H}_{\text{mol}}t} \hat{\boldsymbol{\mu}} \hat{\rho}_{\text{eq}}], \tag{10}$$

where $\text{Tr}[\cdot]$ denotes the trace operation and $\hat{\rho}_{\text{eq}}$ is the equilibrium density matrix.

We assume that the pigment aggregate is in thermal equilibrium before it is excited with light and that the equilibrium state is separable, with the system in its collective electronic ground state, i.e., $\hat{\rho}_{\text{eq}} = |g\rangle\langle g|\hat{\rho}_B^{\text{eq}}$. With this equilibrium state, it is straightforward to show that the dipole–dipole correlation function in Eq. (10) can be written as

$$\langle \mu(t)\mu(0)\rangle = \sum_{m=1}^{N} \sum_{n=1}^{N} \boldsymbol{\mu}_m \cdot \boldsymbol{\mu}_n \text{Tr}_B\left[\langle g|e^{i\hat{H}_{\text{mol}}t}|g\rangle \langle m|e^{-i\hat{H}_{\text{mol}}t}|n\rangle \hat{\rho}_B^{\text{eq}}\right]. \tag{11}$$

Based on Eq. (11), we define the absorption tensor as

$$\text{I}^{\text{A}}(t) = \text{Tr}_B[e^{i\hat{H}_g t} e^{-i\hat{H}_e t} \hat{\rho}_B^{\text{eq}}], \tag{12}$$

where $\hat{H}_g$ and $\hat{H}_e$ are the ground-state and excited-state block of $\hat{H}_{\text{mol}}$, respectively. Absorption spectra $\text{S}^{\text{A}}(\omega)$ are obtained by the Fourier transform of the dipole–dipole correlation function [Eq. (10)]. In terms of the absorption tensor [Eq. (12)], we obtain

$$\text{S}^{\text{A}}(\omega) \propto \omega \sum_{m=1}^{N} \sum_{n=1}^{N} f_{mn}^{\mu,\text{A}} \left[2\text{Re} \int_0^{\infty} dt\, e^{i\omega t} \text{I}_{mn}^{\text{A}}(t)\right], \tag{13}$$

with the dipole factor $f_{mn}^{\mu,\text{A}} = (\boldsymbol{\mu}_m \cdot \boldsymbol{\mu}_n)$.

In a similar way as for the absorption spectrum, the CD spectrum can also be formulated based on a correlation function, this time being the electric dipole–magnetic dipole correlation function. The spectrum $\text{S}^{\text{CD}}(\omega)$ is given by the right-hand side of Eq. (13) with the dipole factor[21]

$$f_{mn}^{\mu,\text{CD}} = \sqrt{\varepsilon_m \varepsilon_n} (\boldsymbol{R}_m - \boldsymbol{R}_n) \cdot (\boldsymbol{\mu}_m \times \boldsymbol{\mu}_n). \tag{14}$$

The LD spectrum, $\text{S}^{\text{LD}}(\omega)$, is also obtained from the right-hand side of Eq. (13). As shown in Appendix A, the dipole factor for LD measurements on disk-shaped pigment aggregates is given by

$$f_{mn}^{\mu,\text{LD}} = \boldsymbol{\mu}_m \cdot \boldsymbol{\mu}_n - 3|\boldsymbol{\mu}_m||\boldsymbol{\mu}_n| \cos\alpha_m \cos\alpha_n, \tag{15}$$

where α_m is the angle between $\boldsymbol{\mu}_m$ and the (uniquely chosen) vector normal to the disk.

C. Absorption tensor

By using an operator identity, Eq. (12) can be written in the time-ordered exponential form as[23]

$$\mathrm{I}^{\mathrm{A}}(t) = \mathrm{Tr}_B\left[\exp_+\left[-i\int_0^t d\tau\, \hat{H}_{eg}(\tau)\right]\hat{\rho}_B^{\mathrm{eq}}\right], \tag{16}$$

with $\hat{H}_{eg}(\tau) = e^{i\hat{H}_g\tau}(\hat{H}_e - \hat{H}_g)e^{-i\hat{H}_g\tau}$. Using Eqs. (2), (5), and (6), we can rewrite Eq. (16) as

$$\mathrm{I}^{\mathrm{A}}(t) = \mathrm{Tr}_B\left[\exp_+\left[-i\left(\hat{H}_S t + \int_0^t d\tau\, \hat{H}_{SB}(\tau)\right)\right]\hat{\rho}_B^{\mathrm{eq}}\right], \tag{17}$$

where $\hat{H}_{SB}(\tau) = e^{i\hat{H}_g\tau}\hat{H}_{SB}e^{-i\hat{H}_g\tau}$. When the system–bath coupling is linear and the bath is harmonic, all the information about the bath that is necessary for the calculation of spectra (both linear and nonlinear) is contained in the correlation function of $\hat{H}_{SB}(t)$,

$$C_n(t) = \sum_{k=1}^{\infty}\omega_k^2 d_{k,nn}^2\langle\hat{q}_k(t)\hat{q}_k(0)\rangle. \tag{18}$$

The correlation function can be determined from its corresponding spectral density $C_n(\omega)$ (see, e.g., Ref. 23) as

$$C_n(t) = \frac{1}{\pi}\int_0^{\infty} d\omega\, C_n(\omega)\frac{\cosh(\beta_{\mathrm{T}}\omega/2 - i\omega t)}{\sinh(\beta_{\mathrm{T}}\omega/2)}, \tag{19}$$

where $\beta_{\mathrm{T}} = \frac{1}{k_B T}$ with k_B being the Boltzmann constant and T being the temperature. The spectral density may be modelled straightforwardly with experimentally motivated parameters (see Sec. III).

1. Full cumulant expansion (FCE)

Since the trace, $\mathrm{Tr}_B[\cdot\,\hat{\rho}^{\mathrm{eq}}]$, amounts to the calculation of a statistical average, it is sensible to expand Eq. (17) in the cumulants of $\hat{H}_{SB}(t)$. Up to second order, such a cumulant expansion yields[18]

$$\mathrm{I}^{\mathrm{A}}(t) = e^{-iH_S t}e^{-K(t)} \tag{20}$$

with

$$K_{\alpha\beta}(t) = \sum_{\delta=1}^{N}\int_0^t d\tau\int_0^{\tau} d\tau'\, e^{i\omega_{\alpha\delta}\tau - i\omega_{\beta\delta}\tau'}C_{\alpha\delta\delta\beta}(\tau - \tau'), \tag{21}$$

where $\omega_{\alpha\delta} = \varepsilon_\alpha - \varepsilon_\delta$ is the energy gap between excitons. If the energy gap fluctuations on different molecules are independent and the correlation functions of all the pigments have the same form [i.e., $C_n(t) = C(t)\,\forall\, n$], we may write

$$C_{\alpha\delta\delta\beta}(t) = \gamma_{\alpha\delta\delta\beta}C(t), \tag{22}$$

with $\gamma_{\alpha\delta\delta\beta} = \sum_{n=1}^{N} c^{n\alpha}c^{n\delta}c^{n\delta}c^{n\beta}$.

It is important to note that the cumulant expansion is a nested expansion; even though only the first two cumulants (mean and variance) are included in the expressions above, the Taylor expansion of $\exp(\cdot)$ involves all orders of H_{SB}. When a distribution is fully described by its first two cumulants (as it is the case for a Gaussian distribution), the cumulant expansion may be (but need not be) exact.

2. Coherent time-dependent Redfield theory (ctR)

The calculation of Eq. (20) can be greatly simplified by making the *secular approximation* and requiring the matrix elements $\langle\alpha|e^{-i\hat{H}_e t}|\beta\rangle$ to be zero for $\alpha \neq \beta$. The cumulant expansion then yields for the absorption tensor[16,19]

$$\mathrm{I}^{\mathrm{A}}_{\alpha\beta}(t) = \delta_{\alpha\beta}e^{-i\varepsilon_\alpha t - g_{\alpha\alpha\alpha\alpha}(t) - \xi_\alpha(t)} \tag{23}$$

with

$$g_{\alpha\alpha\alpha\alpha}(t) = \int_0^t d\tau\int_0^{\tau} d\tau'\, C_{\alpha\alpha\alpha\alpha}(\tau') \tag{24}$$

and

$$\xi_\alpha(t) = \sum_{\beta\neq\alpha}^{N}\int_0^t d\tau\int_0^{\tau} d\tau'\, e^{i\omega_{\alpha\beta}\tau'}C_{\alpha\beta\beta\alpha}(\tau'). \tag{25}$$

In Eq. (23), $g_{\alpha\alpha\alpha\alpha}(t)$ describes pure dephasing, and the real part of $\xi_\alpha(t)$ describes lifetime broadening (see Fig. S2 and the discussion in Secs. IV A and IV B). The imaginary part of $\xi_\alpha(t)$ describes modulation of the exciton energies due to the coupling between exciton states by the off-diagonal system–bath coupling elements.

3. Standard and modified Redfield theories

As stated in Sec. II C 2, the term $\xi_\alpha(t)$ in Eq. (23) accounts for dephasing due to energy relaxation. The same effect can be achieved, phenomenologically, by substituting $\xi_\alpha(t)$ with $R_\alpha t$ for R_α a time-independent rate constant calculated as

$$R_\alpha = \frac{1}{2}\sum_{\beta\neq\alpha}R_{\beta\alpha}, \tag{26}$$

where $R_{\beta\alpha}$ is calculated using standard time-independent Redfield theory,[17]

$$R^{\mathrm{sR}}_{\beta\alpha} = 2\mathrm{Re}\int_0^{\infty} dt\, e^{i\omega_{\alpha\beta}t}C_{\alpha\beta\beta\alpha}(t), \tag{27}$$

or time-independent modified Redfield theory,[24]

$$\begin{aligned}R^{\mathrm{mR}}_{\beta\alpha} = 2\mathrm{Re}\int_0^{\infty} dt\, e^{i\omega_{\alpha\beta}t}\,&\exp\big(-g_{\beta\beta\beta\beta}(t) - g_{\alpha\alpha\alpha\alpha}(t) + g_{\alpha\alpha\beta\beta}(t)\\ &+ g_{\beta\beta\alpha\alpha}(t) - 2i(\lambda_{\alpha\alpha\alpha\alpha} - \lambda_{\beta\beta\alpha\alpha})t\big)\\ &\times\big(C_{\beta\alpha\alpha\beta}(t) - [\dot{g}_{\alpha\beta\beta\beta}(t) - \dot{g}_{\alpha\beta\alpha\alpha}(t) - 2i\lambda_{\alpha\beta\alpha\alpha}]\\ &\times[\dot{g}_{\beta\beta\beta\alpha}(t) - \dot{g}_{\alpha\alpha\beta\alpha}(t) - 2i\lambda_{\beta\alpha\alpha\alpha}]\big),\end{aligned} \tag{28}$$

with $\lambda_{\alpha\beta\gamma\delta} = \sum_{n=1}^{N} c^{n\alpha}c^{n\beta}c^{n\gamma}c^{n\delta}\lambda$ analogous to Eq. (22). The reorganization energy can be calculated from the spectral density as $\lambda = \int_{-\infty}^{\infty}\frac{d\omega}{2\pi\omega}C(\omega)$.

Note that the upper limit of integration in Eqs. (27) and (28) is $t \to \infty$, and these expressions, therefore, describe the Markovian long-time Redfield and modified Redfield rates.

As in Sec. II C 2, the secular approximation was invoked in the derivation of the Redfield and modified Redfield rates above. It is well known that the non-secular Redfield relaxation tensor may

lead to positivity breakdown in the excited state population dynamics, while the secular form in Eq. (27) (as the so-called Lindbladian) yields strictly positive populations. When calculating linear spectra, the non-positivity may not be problematic, since the coherence block of the density matrix, which takes part in the evaluation of the linear spectra, evolves independently of the block of excited state dynamics. Although often quantitatively incorrect, the non-secular Redfield rates shows the right qualitative behavior in describing non-secular effects in the linear spectra.[25] The secular approximation may significantly decrease the size of the computational problem, especially for large pigment aggregates, however, and is therefore used in this study.

The Redfield rate in Eq. (27) is a purely real quantity, while the corresponding ctR term in Eq. (25) is complex. The latter was first derived from the Partial Ordering Prescription (POP) in Ref. 16. By application of the Markov approximation to the ctR expression, a complex time-independent quantity

$$R^{\mathrm{POP}}_{\beta\alpha} = R^{\mathrm{sR}}_{\beta\alpha} + iR^{\mathrm{imag}}_{\beta\alpha} \tag{29}$$

is found,[16] from which $\xi_\alpha(t)$ can be calculated via Eq. (26). The imaginary contribution to $R^{\mathrm{POP}}_{\beta\alpha}$ can be obtained from a Kramers–Kronig relation with the real Redfield rate as

$$R^{\mathrm{imag}}_{\beta\alpha} = \gamma_{\alpha\beta\beta\alpha} \cdot \frac{1}{\pi}\mathcal{P}\int_{-\infty}^{\infty} d\omega \frac{R^{\mathrm{sR}}(\omega)}{\omega_{\alpha\beta} - \omega}, \tag{30}$$

with $R^{\mathrm{sR}}(\omega) = 2\mathrm{Re}\int_0^\infty dt\, e^{i\omega t} C(t)$, analogous to Eq. (27), and $\mathcal{P}(\cdot)$ denoting the Cauchy principal value. In this article, we will call this complex extension to the Redfield method the time-independent POP method.

4. Exact stochastic path integral evaluation (PI)

It may well be impossible to find an exact closed expression for the absorption tensor. Exact calculations can, however, be performed by Monte Carlo path integration.[15] In this method, Eq. (17) is considered as the average (indicated by $\mathrm{Tr}_B[\cdot]$) of many solutions of the equation

$$\frac{d}{dt}\rho^{\mathrm{A}}(t) = -i\left(\hat{H}_S + \sum_{n=1}^{\infty}\xi_n(t)|n\rangle\langle n|\right)\rho^{\mathrm{A}}(t), \tag{31}$$

subject to the initial condition $\rho^{\mathrm{A}}(0) = \hat{I}$, where $\hat{I}$ is the identity operator in the system's Hilbert space. In Eq. (31), $\xi_n(t)$ is a stochastic process conforming to the statistics of $\hat{H}_{SB}(t)$, namely,

$$\begin{aligned}\langle \xi_m(t)\xi_n(t')\rangle &= \delta_{mn}C_n(t-t'),\\ \langle \xi_n(t)\rangle &= 0.\end{aligned} \tag{32}$$

The absorption tensor is calculated as the average of many stochastic solutions of Eq. (31),

$$\mathrm{I}^{\mathrm{A}}(t) = \langle \rho^{\mathrm{A}}(t)\rangle_\xi. \tag{33}$$

As shown in Ref. 15, this average converges to the exact absorption tensor as the number of stochastic trajectories increases to infinity.

III. METHODS

A. Molecular system

For the calculations in this study, we consider a molecular dimer with a single electronic transition on each molecule. For the sake of computational convenience, we subtract the energy of the lower frequency electronic transition from the energies of the excited states, which amounts to applying the so-called Rotating Wave Approximation (RWA). This allows us to reduce the problem to just the treatment of the excited state block of the Hamiltonian, which then takes the form

$$H_S = \begin{bmatrix}\epsilon & J\\ J & 0\end{bmatrix}, \tag{34}$$

where ϵ is the site basis energy gap between the electronic transitions on the two molecules of the dimer, and J is their resonance coupling.

The exact method of stochastic path integration (PI; see Sec. II C 4) is significantly more tractable for the calculation of linear spectra than using the Hierarchical Equations of Motion (HEOM), as was done in earlier works.[14,19] Nevertheless, the convergence of PI calculations slows precipitously as more high-frequency modes are added to the bath. In order for PI convergence to be sufficient, as well as for our conclusions to be valid for real systems, we describe the bath by a spectral density with contributions from a continuum of phonon modes and eight intramolecular vibrations. We assume that all the pigment molecules have the same correlation function. The low-frequency phonon contribution is modeled as a quantum Brownian oscillator with parameters used in earlier studies,[6,26]

$$C_{\mathrm{ph}}(\omega) = 2\lambda_{\mathrm{ph}}\frac{\omega\gamma_{\mathrm{ph}}}{\omega^2 + \gamma_{\mathrm{ph}}^2}, \tag{35}$$

with the reorganization energy $\lambda_{\mathrm{ph}} = 40\ \mathrm{cm}^{-1}$ and spectral width $\gamma_{\mathrm{ph}} = 40\ \mathrm{cm}^{-1}$. The high-frequency part of the spectral density is implemented as the sum of underdamped modes[20] with parameters of the first eight high-frequency modes of the plant light-harvesting complex LHCII[27] (see Table I), which are predominantly due to chlorophyll *a* vibrations of the lowest-energy exciton

$$C_{\mathrm{hf}}(\omega) = \sum_{i=1}^{8}\frac{\omega_i|\omega_i|S_i\gamma_i}{2\left((|\omega| - \omega_i)^2 + \left(\frac{\gamma_i}{2}\right)^2\right)}, \tag{36}$$

with $\gamma_i = 6\ \mathrm{cm}^{-1}\,\forall\, i$, and the central frequencies (ω_i) and Huang–Rhys factors (S_i) given in Table I.

B. Evaluation of spectra

We evaluated approximate spectra by comparing them to the exact spectra determined from PI using the quality factor defined by Gelzinis *et al.*[19] as a measure of the correctness of an approximate spectrum,

$$Q = \frac{\int_{-\infty}^{\infty} d\omega\left(S^{\mathrm{PI}}(\omega) \cap S^{\mathrm{approximate}}(\omega)\right)}{\int_{-\infty}^{\infty} d\omega\left(S^{\mathrm{PI}}(\omega) \cup S^{\mathrm{approximate}}(\omega)\right)}, \tag{37}$$

where S^{PI} and $S^{\mathrm{approximate}}$ are the normalized spectra obtained from PI and an approximate method, respectively. In Eq. (37), $\cap$ and $\cup$ denote the intersection and union of spectra, respectively.

TABLE I. Central frequency ω and Huang–Rhys factor S for each of the underdamped modes used in this study. These modes correspond to the first eight high-frequency modes of LHCII as determined from fluorescence line-narrowing spectra.[27] The Huang–Rhys factors were scaled by a factor of 0.8 to better fit experimental spectra.[6]

ω_i (cm^{-1})	97	138	213	260	298	342	388	425
S_i	0.0192	0.0230	0.0240	0.0214	0.0214	0.0483	0.0199	0.0119

C. Dipole factors

All the absorption-type spectra (OD, LD, and CD) can be obtained from the absorption tensor $\mathrm{I}^{\mathrm{A}}(t)$ by element-wise multiplication with the relevant symmetrical dipole factor matrix f_{mn} [see Eqs. (13)–(15)]. Since the spectra were normalized when calculating quality, only the ratio of the dipole matrix elements is important. For simplicity, we omitted the frequency and energy prefactors in Eqs. (13) and (14) when calculating spectra. For the most part, we consider the following four dipole factor matrices in our calculations:

$$f_{0,1}^{1,0} = \begin{bmatrix} 1 & 0 \\ 0 & 1 \end{bmatrix}, \qquad f_{1,1}^{1,1} = \begin{bmatrix} 1 & 1 \\ 1 & 1 \end{bmatrix}, \qquad f_{-1,0}^{1,-1} = \begin{bmatrix} 1 & -1 \\ -1 & 0 \end{bmatrix}, \quad \text{and} \quad f_{1,0}^{0,1} = \begin{bmatrix} 0 & 1 \\ 1 & 0 \end{bmatrix}, \tag{38}$$

where $f_{0,1}^{1,0}$ and $f_{1,1}^{1,1}$ correspond to absorption spectra when the two dipole moments of the dimer have equal strength and are orthogonal and parallel to each other, respectively, $f_{-1,0}^{1,-1}$ corresponds to an LD spectrum with $\boldsymbol{\mu}_1$ a unit vector orthogonal to the LD axis (see Appendix A), $\boldsymbol{\mu}_2$ at the magic angle (54.7°) relative to the LD axis, and $\boldsymbol{\mu}_1 \cdot \boldsymbol{\mu}_2 = -1$, and $f_{1,0}^{0,1}$ is the dipole factor for CD.

Note that the secular approximation is almost fully valid for the dipole factor $f_{0,1}^{1,0}$, for which Eq. (13) amounts to a trace over the (Fourier-transformed) absorption tensor. The trace is basis-independent and therefore depends only on the diagonal elements of the secular absorption tensor in the exciton basis. Transfer between these diagonal tensor elements is calculated secularly for the ctR, Redfield, and modified Redfield methods but corresponds very well with interdiagonal transfer for the nonsecular FCE method, as shown in Sec. IV B.

D. Numerical implementation for the calculation of absorption tensors

To incorporate inhomogeneous disorder, site energies were drawn independently from a normal distribution with a FWHM of 140 cm^{-1} (a value that is often used in literature for light-harvesting complexes[28–30]) and centered on the applicable energies. An ensemble size of 5000 was used for disordered calculations of approximate spectra.

For the PI method, disorder sampling commutes with Monte Carlo integration.[15] The noise trajectories [$\xi_n(t)$ in Eq. (31)] were calculated using the procedure described by Moix *et al.*,[15] and the stochastic integration was performed in the site basis with the second-order weak technique described in Appendix B. We found the second-order weak technique significantly more accurate than the first-order strong Milstein method. Weak and strong approximations guarantee convergence of the statistical moments and of individual trajectories, respectively, to a certain order—see Kloeden and Platen[31] for an extensive discussion of stochastic differential equations and their solution.

For a harmonic bath and linear system–bath coupling (see Sec. II C 4), spectra calculated with the PI method converge to the exact spectra. To ensure that convergence was sufficient, two independent PI calculations were performed for each parameter set in Sec. IV, and the relative quality of the two obtained spectra was determined by substituting one of the spectra for $S^{\text{approximate}}$ and the other for S^{PI} in Eq. (37). The results of this convergence test are shown in Figs. S11 and S12. The independent calculations agreed within ~1%, ~1.5%, and ~2% for absorption, LD, and CD spectra, respectively, with convergence being least optimal for small couplings. Since both of the independent calculations deviated from the exact spectrum, the true convergence is expected to be better than that shown in Figs. S11 and S12. The trends identified in Sec. IV occur on quality scales much larger than the expected deviation of the PI spectra from the true spectra, and these trends are therefore statistically significant. The calculated tensors were visually inspected and truncated when decay was almost complete (at about 180 and 270 fs for calculations at 300 and 100 K, respectively). The approximate tensors were truncated at the same time points and all signals were subsequently zero-padded before calculating spectra by Fourier transformation [see Eq. (13)].

Although Eqs. (20) and (21) can be used to calculate the FCE absorption tensor directly, we used the computationally less expensive approach introduced and discussed in Ref. 21. We summarize this approach briefly below. For our dimer system, Eq. (21) can be written as

$$K_{\alpha\beta}(t) = \sum_{\delta=1}^{2}\sum_{n=1}^{2} X_n^{\alpha\delta} X_n^{\delta\beta} F_{\alpha\delta\beta}(t) \tag{39}$$

with $X_n^{\alpha\delta} = (c^{n\alpha})^* c^{n\delta}$ and

$$F_{\alpha\delta\beta}(t) = \int_0^t d\tau \int_0^\tau d\tau'\, e^{i\omega_{\alpha\delta}\tau - i\omega_{\beta\delta}\tau'} C(\tau - \tau'). \tag{40}$$

By using integration by parts, Eq. (40) is reformulated as

$$F_{\alpha\delta\beta}(t) = \begin{cases} tG_{\alpha\delta}(t) - H_{\alpha\delta}(t) & (\omega_{\alpha\beta} = 0), \\ \dfrac{e^{i\omega_{\alpha\beta}t}}{i\omega_{\alpha\beta}} G_{\beta\delta}(t) - \dfrac{1}{i\omega_{\alpha\beta}} G_{\alpha\delta}(t) & (\omega_{\alpha\beta} \neq 0), \end{cases} \tag{41}$$

with $G_{\beta\delta}(t) = \int_0^t e^{i\omega_{\beta\delta}\tau} C(\tau) d\tau$ and $H_{\alpha\delta}(t) = \int_0^t \tau e^{i\omega_{\alpha\delta}\tau} C(\tau) d\tau$. To use the method above, we precalculated the integrals $\int_0^t e^{i\omega\tau} C(\tau) d\tau$ and

$\int_0^t \tau e^{i\omega\tau} C(\tau) d\tau$ for a grid of frequencies ω and time points t, making sure that both time and frequency were sampled sufficiently (i.e., that a denser or more extended sampling did not yield significantly different results). We then interpolated these integrals in ω to calculate the absorption tensor for each realization of the disorder. The time points were chosen such that the frequency axis of the Fourier transformation allowed the representation of the full spectrum. The ctR, Redfield, modified Redfield, and independent POP calculations were performed by evaluating Eq. (23) with $\xi_\alpha(t)$ calculated from Eqs. (25) and (27)–(29), respectively, with $\alpha, \beta \in \{1, 2\}$. The integrals in Eqs. (24), (25), and (27) were precalculated in a similar fashion as described above for FCE. The approximate absorption tensors were calculated in the exciton basis and then transformed to the site basis using the transformation

$$\mathrm{I}^{\mathrm{site}}(t) = \Lambda \mathrm{I}^{\mathrm{ex}}(t) \Lambda^\dagger, \tag{42}$$

with $\Lambda_{n\alpha} = c^{n\alpha}$ and $(\cdot)^\dagger$ denoting Hermitian conjugation.

IV. RESULTS AND DISCUSSION

A. Dependence of spectral quality on site energy gap and excitonic coupling

In order to determine the accuracy of the approximate methods for different Hamiltonians, we varied ϵ and J in Eq. (34) independently in the ranges $[0, 500]$ and $[-55, 55]$ cm^{-1}, respectively. The obtained qualities for inhomogeneously broadened absorption-type spectra are shown in Fig. 1 for different dipole factors at 300 K. Spectra of selected coupling–energy gap pairs (indicated for the FCE qualities in Fig. 1) are shown in Fig. 2.

It is clear from Fig. 1 that absorption-type spectra calculated with FCE are more accurate than spectra calculated with any of the other methods for the dipole factors in this figure. The quality of these FCE spectra is practically independent of the site energy gap and coupling, and spectra for systems with many pigments (i.e., many different site energies and couplings) may therefore be calculated with predictable quality.

In Sec. II C 1, we noted that the second-order cumulant expansion may be exact when $\hat{q}(t)$ in Eq. (18) is a Gaussian process. This expansion indeed leads to exact expressions in the case of a monomeric system (or polymeric system with no interpigment coupling), when the bath is harmonic and $\hat{H}_{\mathrm{SB}}$ is linear in system and bath operators. Since all of the approximate methods were derived using the second-order cumulant expansion, this perfect correspondence can be seen in Figs. 1(a), 1(b), and 1(d) for all the methods at zero coupling. The perfect agreement of spectra is also seen in Fig. 2(b), where spectra for the different methods are shown for the coupling–energy gap pair $(0, 500)$ cm^{-1} and the dipole factor $f_{1,1}^{1,1}$. The case for the coupling being exactly zero is not shown for CD qualities [Fig. 1(c)] since CD spectra are then identically zero.

For an excitonically coupled system, the cumulant expansion is exact for the treatment of fluctuations induced by the diagonal elements of the system–bath coupling Hamiltonian in the exciton basis. It is not exact for fluctuations induced by the off-diagonal elements; however, since the terms that depend on these elements also include excitonic propagators $e^{i\omega_{\alpha\beta}t}$ [see Eqs. (24) and (25)].[19] Despite the second-order truncation, the FCE method is remarkably accurate for the calculation of most spectra in the considered site energy gap and coupling ranges, as seen in Figs. 1(a), 1(b), and 1(d). Only for the CD spectrum [Fig. 1(c)], when the anti-diagonal dipole factor prescribes significant inclusion of off-diagonal system–bath coupling effects (see Sec. IV C), and the second-order truncation is therefore least accurate, is the quality of FCE absorption-type spectra notably worse than for the exact approach.

The secular approximation is made in the derivation of the ctR, Redfield, and modified Redfield methods but not in the derivation of the FCE method. In fact, this approximation is the only difference between the FCE and ctR methods. For secular methods, the off-diagonal elements of the absorption tensor [Eq. (12)] are zero in the exciton basis. The discrepancy in quality between FCE and ctR spectra, therefore, depends on the contribution of these off-diagonal (i.e., nonsecular) elements to the FCE spectra. The spectral contribution from the nonsecular elements depends on both the dipole factor and the system–bath coupling Hamiltonian.

As discussed in Sec. III, the dipole factor $f_{0,1}^{1,0}$ corresponds to the calculation of a nonsecular spectrum, also for secular methods. The isolated effect of the dipole factor on the quality of absorption spectra is seen in Figs. 1(a) and 1(b), where the secular approximation is fully valid for Fig. 1(a) (see Sec. III), while, for the same dipole strengths, it is least accurate for Fig. 1(b). The dependence of the spectra on the dipole factor also causes the poor quality of the secular CD spectra seen in Fig. 1(c), since the CD dipole factor, $f_{1,0}^{0,1}$, corresponds poorly with $f_{0,1}^{1,0}$. A detailed discussion of the dependence of spectral accuracy on the dipole factor is given in Sec. IV C.

When the system–bath coupling is treated within the secular approximation, it induces population relaxation but not transfer between exciton populations and coherences, and the off-diagonal elements of the secular absorption tensors therefore remain zero. Such nonsecular transfer dynamics, when considered, would influence the exciton structure by changing the contribution of sites to exciton states in a process called the dynamic localization of excitons.[32] For the FCE method, nonsecular contributions are due to bath correlation functions of the form $C_{\alpha\beta\beta\beta}$ or $C_{\alpha\alpha\alpha\beta}$. The factor $\gamma_{\alpha\beta\beta\beta}$ defining these correlation functions [see Eq. (22)] is small for small site energy gaps and weak couplings (Fig. S1), and for these parameters the qualities of ctR spectra are therefore almost as high as the qualities of FCE spectra [see Figs. 1(b) and 1(d)]. The quality of CD spectra calculated with the ctR method also corresponds best with FCE qualities at small site energy gaps but (as discussed in Sec. IV B) CD spectra depend strongly on nonsecular elements when the coupling is weak, so that the ctR qualities differ significantly from the FCE qualities for weak coupling. The high accuracy of the secular approximation for small site energy gaps and weak couplings is contrary to the expectation[20,29] that the negative effects of neglected dynamic localization on spectral quality are strongest under these conditions. CD spectra calculated with the ctR, Redfield, or modified Redfield methods are impacted considerably by both the second-order truncation in the cumulant expansion and by the secular approximation, and their quality is poor for all site energy gaps and couplings considered in Fig. 1.

The quality of absorption-type spectra calculated using the Redfield method depends similarly on the site energy gap and coupling as the quality of modified Redfield spectra. As shown in Fig. 1, these methods yield spectra that are less accurate than FCE and

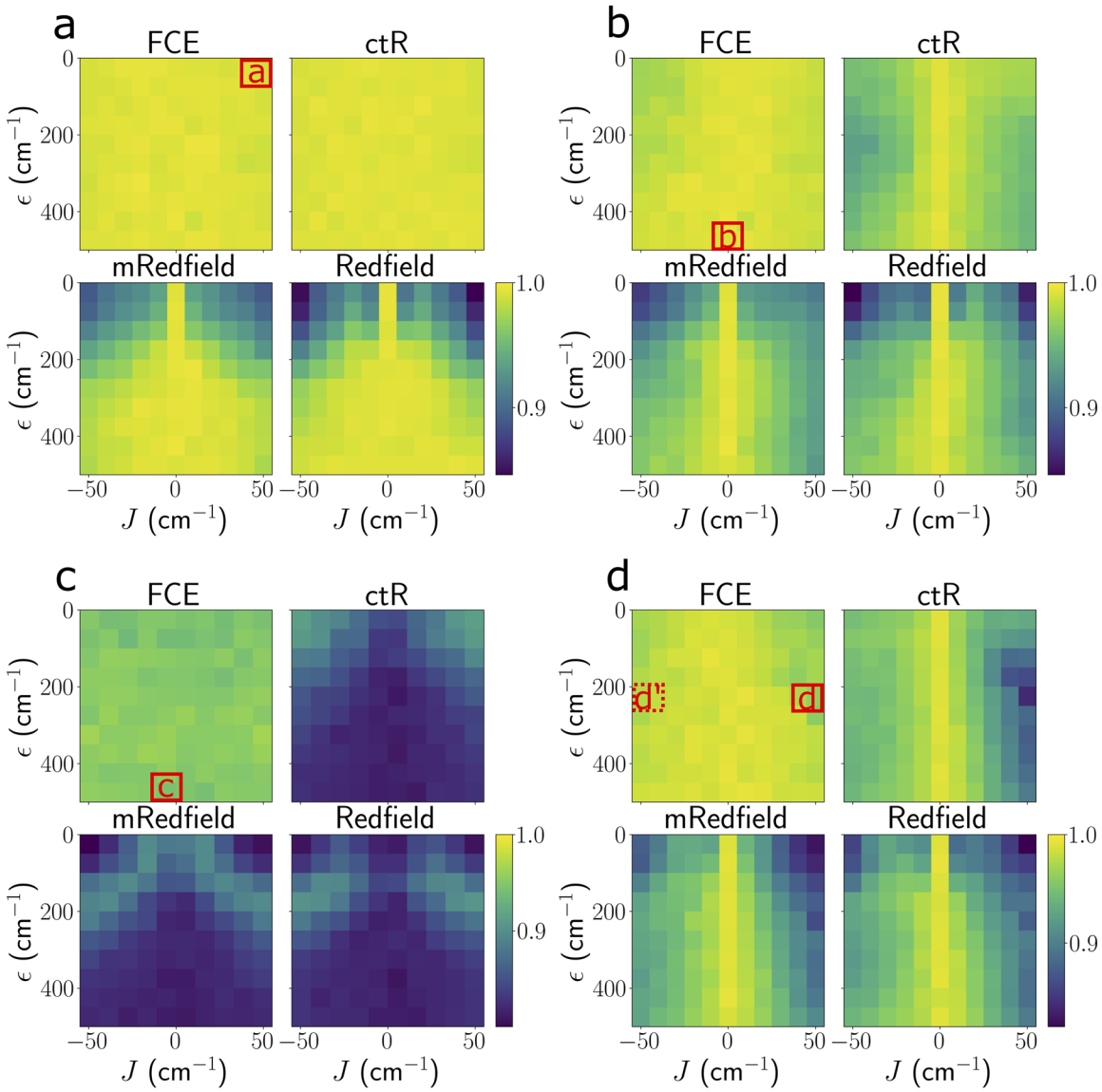

FIG. 1. Dependence of the quality of absorption-type spectra on the site energy gap ϵ and coupling J at 300 K. Qualities are shown for the absorption dipole factors (a) $f_{0,1}^{1,0}$ and (b) $f_{1,1}^{1,1}$, (c) the CD dipole factor $f_{1,0}^{0,1}$, and (d) the LD dipole factor $f_{-1,0}^{1,-1}$. A disorder of $\sigma_{\mathrm{FWHM}} = 140\ \mathrm{cm}^{-1}$ was used for the calculation of spectra. The coupling–energy gap pairs for which spectra are shown in Fig. 2 are indicated with red frames and the inscribed labels correspond with the respective labels in Fig. 2.

ctR spectra. The difference between the former pair of spectra and ctR spectra (which serve as proxy for the more accurate spectra) is most pronounced at small site energy gaps and strong coupling. The reason for this difference is the energy shift and narrowing of Redfield and modified Redfield spectra relative to ctR spectra, as seen in Fig. 2(a) for the coupling–energy gap pair $(55, 0)\ \mathrm{cm}^{-1}$ and dipole factor $f_{0,1}^{1,0}$. These spectral differences are due to the fact that the Redfield and modified Redfield rates in Eqs. (27) and (28) are real quantities, whereas the corresponding term, $\xi(t)$, in Eq. (25) is complex.[19] Figure S2 shows the Redfield and long-time ctR rates that were not corrected for pigment participation in excitons [i.e., $\gamma_{\alpha\beta\beta\alpha}$ was set equal to 1 in Eq. (22)]. As seen in this figure, the imaginary rate-induced energy splitting in ctR spectra increases with the difference between exciton energies (exciton gap) for small exciton gaps, while the rate-induced spectral shift stays fairly constant at a value of about 30 cm^{-1} [see Fig. S2 and Fig. 2(a)]. Although the rate-induced splitting in ctR spectra decreases momentarily for exciton gaps larger than about 35 cm^{-1}, the disorder-averaged participation factor $\gamma_{\alpha\beta\beta\alpha}$ increases with coupling strength for fixed energy (see Fig. S1), and the resultant effect is the worsening of Redfield and modified

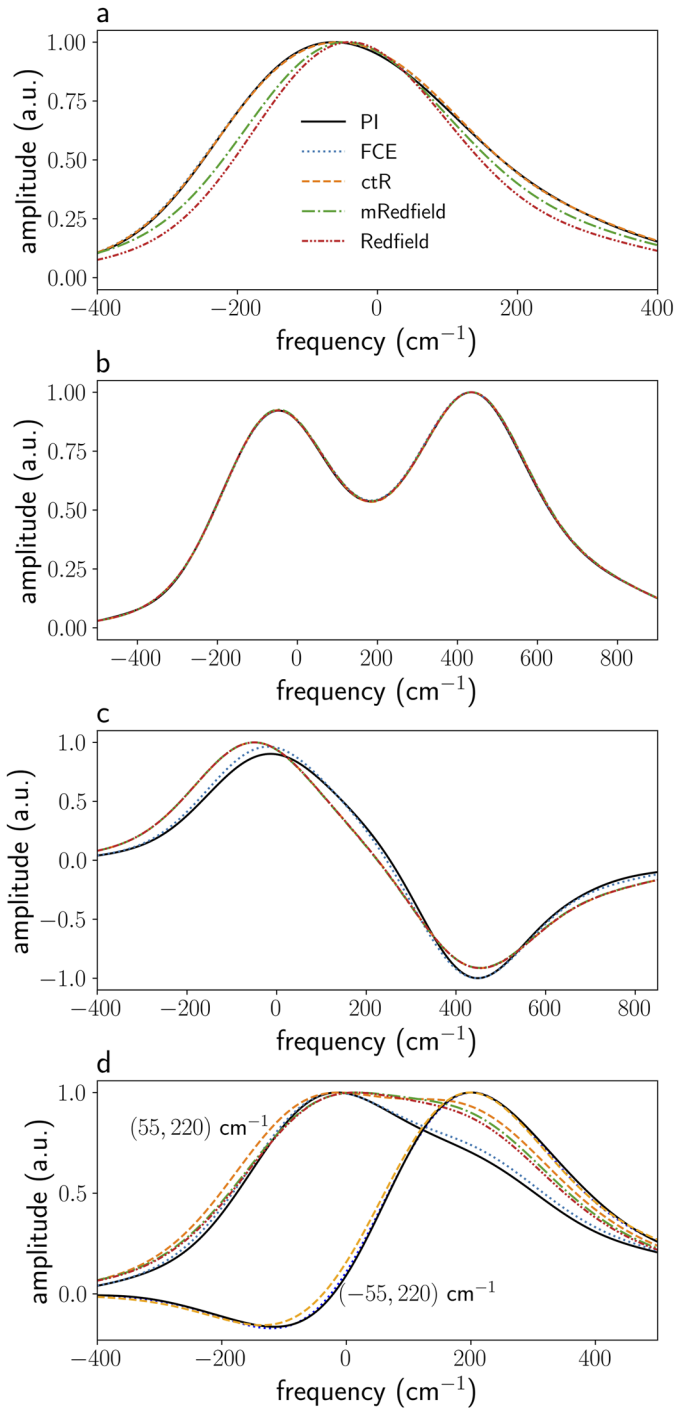

FIG. 2. Absorption-type spectra for selected coupling–energy gap pairs and dipole factors, as indicated in Fig. 1. Spectra are shown for the dipole factors and coupling-energy pairs (a) $f^{1,0}_{0,1}$; $(55, 0)$ cm^{-1}, (b) $f^{1,1}_{1,1}$; $(0, 500)$ cm^{-1}, (c) $f^{0,1}_{1,0}$; $(-11, 500)$ cm^{-1}, and (d) $f^{1,-1}_{-1,0}$; $(\pm 55, 220)$ cm^{-1}. The same parameters were used for the generation of spectra as were used in Fig. 1. The spectra for the coupling–energy gap pairs $(55, 220)$ and $(-55, 220)$ cm^{-1} refer to points *d* and *d′*, respectively, in Fig. 1.

Redfield qualities with increasing coupling strength, especially for small site energy gaps. Note that the participation factor, $\gamma_{\alpha\beta\beta\alpha}$, is a noncontinuous function of coupling strength at zero site energy gap when inhomogeneous disorder is not included (it has a value of 0 for zero coupling and 0.5 otherwise). When inhomogeneous disorder is accounted for realistically at small site energy gaps, however, $\gamma_{\alpha\beta\beta\alpha}$ is a smooth function of the coupling strength, and the phenomenological inclusion of dynamic localization in the theory[20,29] is therefore not necessary to counteract excessive delocalization. Based on the (already) good agreement between the secular ctR and nonsecular FCE spectra at small site energy gaps, such attempts to account for nonsecular effects will likely not improve the quality of Redfield and modified Redfield spectra. Although the exciton gap is largest for the largest values of the site energy gap and coupling in Fig. 1, the excitons for these parameters are strongly localized (as seen from the small values for $\gamma_{\alpha\beta\beta\alpha}$ in Fig. S1) and the population transfer rates between excitons are therefore small. Figure 1(a) shows that the qualities of Redfield and modified Redfield spectra improve markedly with the magnitude of the site energy gap, due to the diminishing contribution from population transfer rates. In contrast to the results of Gelzinis *et al.*, the modified Redfield method performs slightly better than the Redfield method for the parameters considered in Fig. 1.

The qualities in Fig. 1 are generally symmetric in the coupling between sites, but some asymmetries are apparent, the most noticeable of which is the asymmetry between the coupling–energy gap pairs $(55, 220)$ and $(-55, 220)$ cm^{-1} for the LD qualities in Fig. 1(d). In Fig. 2(d), spectra from all the methods are shown for the parameters $(55, 220)$ cm^{-1}, and the PI, FCE, and ctR spectra are shown for the parameters $(-55, 220)$ cm^{-1}. Although the exciton energies, pigment participations, $(c^{n\alpha})^2$ (but not $c^{n\alpha}$), and dipole factor are the same for these two coupling–energy gap pairs, the spectra differ significantly. As discussed in Sec. III, the dipole factor, $f^{1,-1}_{-1,0}$, used in Fig. 1(d) corresponds to an LD measurement of a dimer in which the high-energy pigment is orthogonal to the LD axis and the other pigment is at the magic angle with the LD axis. For $(-55, 220)$ cm^{-1}, the high-energy exciton contributes most intensely to the spectrum. For $(55, 220)$ cm^{-1}, however, the spectral contribution is most intense for the exciton to which the LD-forbidden low-energy pigment contributes predominantly. This borrowing of excitation directly illustrates excitonic quantum superposition between states of local excitation and shows the principle by which forbidden transitions can be probed through their coupling with allowed transitions. Notice that the secular spectra differ significantly from PI and FCE spectra for $(55, 220)$ cm^{-1}, which indicates that nonsecular transfer effects are important when excitons cannot be excited directly through interaction with light.

The dependence of the spectral quality on the site energy gap and coupling at 100 K is qualitatively very similar to the dependence shown in Fig. 1. An image plot of spectral qualities at 100 K, similar to Fig. 1, is shown in Fig. S3.

B. Dependence of spectral quality on the excitonic energy gap

For calculations in this section, the site energy gap was varied for fixed values of the excitonic coupling. For each site energy gap, the excitonic energy gap was calculated as the difference between

exciton energies. Figure 3 shows the quality of inhomogeneously broadened approximate absorption-type spectra as a function of the excitonic energy gap at 300 K for $J = 15$ cm^{-1} (an average value in antenna complexes of plants) and $J = 100$ cm^{-1} (a strong coupling for these complexes). The high-frequency spectral density is also included in these figures and was multiplied by a factor $1/\omega^2$ so that the peak heights of the underdamped modes are proportional to their Huang–Rhys factors. As discussed in Sec. III, these underdamped modes correspond to the first eight (from a total of 48) high-frequency vibrations of LHCII, which are mostly due to intramolecular vibrations in the chlorophyll *a* molecule. The sixth vibrational mode has the largest Huang–Rhys factor of all the modes of LHCII, and the spectral density considered in this article is therefore a good model of the system–bath coupling in a complex system like LHCII.

It is clear from Fig. 3 that, at 300 K, the FCE method produces accurate spectra for moderate ($J = 15$ cm^{-1}) and strong ($J = 100$ cm^{-1}) coupling for all of the considered dipole factors.

For moderate coupling, the ctR absorption and LD spectra of which the qualities are shown in Figs. 3(a), 3(b), and 3(d) deviate less than 4% from the exact spectra, and the quality of these spectra is nearly constant over the range of exciton energy gaps considered in Fig. 3.

The quality of Redfield and modified Redfield spectra corresponds almost exactly with the quality of ctR spectra at excitonic energy gaps larger than about 250 cm^{-1} for moderate coupling. As discussed in Sec. IV A, the excitons are localized at large energy gaps and differences between the rate calculations for these methods have a negligible effect. For strong coupling, the difference in accuracy between ctR spectra and Redfield-type spectra also decreases with exciton gap, but is still present for large gaps in Fig. 3, since excitons are not yet fully localized when the coupling is strong. The inaccuracy in the calculation of Redfield and modified Redfield spectra may lead to their quality being incidentally better than for ctR spectra [Figs. 3(c) and 3(d)].

The quality of absorption-type spectra at 100 K (Fig. S4) depends similarly on the excitonic energy gap as the quality at 300 K, although at 100 K, the Redfield and modified Redfield methods produce even poorer qualities for small exciton energy gaps than they do at 300 K.

The quality of spectra calculated with zero disorder is shown in Fig. S5 (for $T = 100$ K and $J = 100$ cm^{-1}) and Fig. S6 (for $T = 300$ K and $J = 15$ cm^{-1}). For each coupling strength, the overall accuracy of these spectra depends similarly on the excitonic energy gap as the accuracy for inhomogeneously broadened spectra. For zero disorder, however, spectra calculated with the Redfield method are significantly less accurate than inhomogeneously broadened spectra when the energy gap is resonant with intramolecular modes. No decrease in accuracy around resonance frequencies is seen for any of the other methods in Figs. S5 and S6. For the calculation of modified Redfield rates, the Fourier-transformed correlation function is convoluted with the Fourier transform of several other time-dependent functions [see Eq. (28)], and the accuracy, therefore, depends more smoothly on the frequency. The sensitivity of Redfield spectra to resonance agrees well with the results obtained by Gelzinis *et al.*,[19] where the authors used a single intramolecular mode with reorganization energy $\lambda = 15$ cm^{-1}, comparable to the reorganization energy of ≈17 cm^{-1} of the sixth mode in our study. The insensitivity of

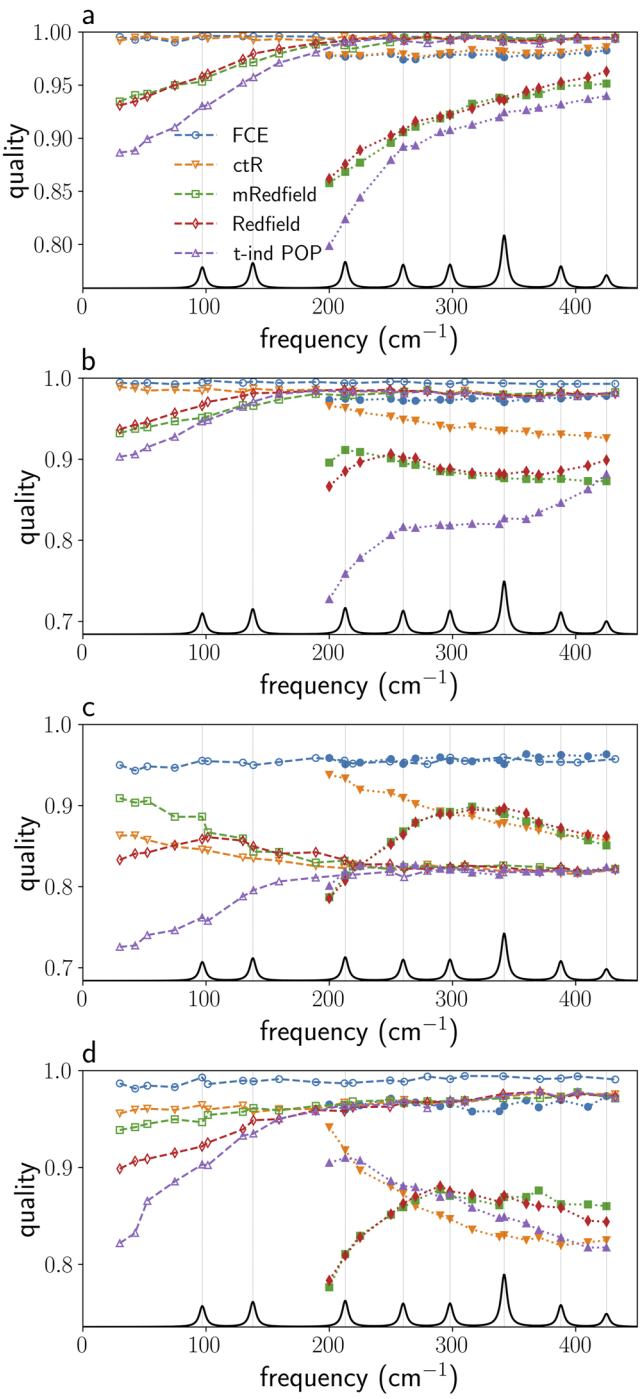

FIG. 3. Quality of absorption-type spectra at 300 K for excitonic coupling $J = 15$ cm^{-1} (open markers) and $J = 100$ cm^{-1} (filled markers) as a function of the excitonic energy gap. Qualities are shown for the absorption dipole factors (a) $f_{0,1}^{1,0}$ and (b) $f_{1,1}^{1,1}$, (c) CD dipole factor $f_{1,0}^{0,1}$, and (d) LD dipole factor $f_{-1,0}^{1,-1}$. A disorder of $\sigma_{\mathrm{FWHM}} = 140$ cm^{-1} was used for the calculation of spectra. Note that the smallest possible excitonic energy gap equals 2*J*. The peak heights of the high-frequency spectral density (black line) are proportional to the Huang–Rhys factors of the intramolecular modes.

modified Redfield qualities to resonance is in contrast to the small but significant decrease in quality seen by Gelzinis *et al.* around the resonance frequency in their study. When using a single-mode spectral density with the parameters of Gelzinis *et al.*, we found the quality of modified Redfield spectra to indeed be lowest at resonance (not shown), but the quality was less sensitive to the excitonic energy gap than what was reported by Gelzinis *et al.*, likely due to the different forms used for the underdamped modes in our study and theirs [compare Eq. (36) with Eq. (31) in their article[19]]. For the full spectral density used in our study, the insensitivity of the modified Redfield quality to resonance with a particular underdamped mode may be attributed to the convoluting influence of the other modes.

As discussed in Sec. II C 3, the Redfield and modified Redfield methods depend on the long-time rates—the integrands in Eqs. (27) and (28) may persist for several picoseconds, especially at low temperature. For the temperatures considered in this study, however, the absorption tensor decays in a few hundred femtoseconds and the short-time dynamics of population transfer are therefore important. The necessity of accurately accounting for the short-time dynamics is illustrated by the fact that the quality of spectra calculated using the complex time-independent POP method (see Fig. S2 and the discussion below) is also strongly sensitive to resonance with intramolecular modes (not shown). The non-Markovianity of methods, and not merely the presence of imaginary contributions, therefore helps to prevent sensitivity of spectra to resonance with intramolecular modes.

Figure 3 shows the quality of spectra calculated using the complex time-independent POP method (see Sec. II C 3). A surprising observation is that this complex method generally performs worse than its real counterpart—the Redfield method. As shown in Fig. S9 for parallel dipole moments, the time-independent POP method shifts the single-exciton Redfield spectrum uniformly, whereas the complex rate contribution from non-Markovian methods (PI, FCE, and ctR) may broaden the spectrum without causing a significant shift. From the time-independent POP qualities in Fig. 3, it is clear that non-Markovianity of a method is crucial for its accuracy.

The sensitivity of quality to resonance is significantly reduced at 300 K and $J = 15\ \mathrm{cm}^{-1}$ (Fig. S6), when the weaker coupling causes localization already for small exciton gaps. When inhomogeneous disorder is treated realistically, the accuracy of spectra is independent of resonance with intramolecular modes and is therefore of no concern for the calculation of disordered bulk absorption-type spectra in plant light-harvesting complexes.

As discussed in Sec. IV A, correlation functions of the form $C_{\alpha\beta\beta\beta}$ in Eq. (21) are zero for the site energy gap being zero (corresponding to the smallest exciton gap) and nonsecular effects are therefore absent. For this reason, the ctR and FCE methods correspond exactly for the smallest exciton gap when the disorder is zero.

In the PC645 complex of cryptophyte algae[33,34] and in the LH2 complex of purple bacteria,[33,35] the interpigment coupling may be as high as 320 and 560 cm^{-1}, respectively, and extending our discussion to very strong couplings is therefore useful. To that end, the qualities for $J = 100$, 300, 500, and 750 cm^{-1} are shown in Fig. 4 as functions of the excitonic energy gap for $T = 300$ K (notice that we used offsets in qualities for $J > 100\ \mathrm{cm}^{-1}$).

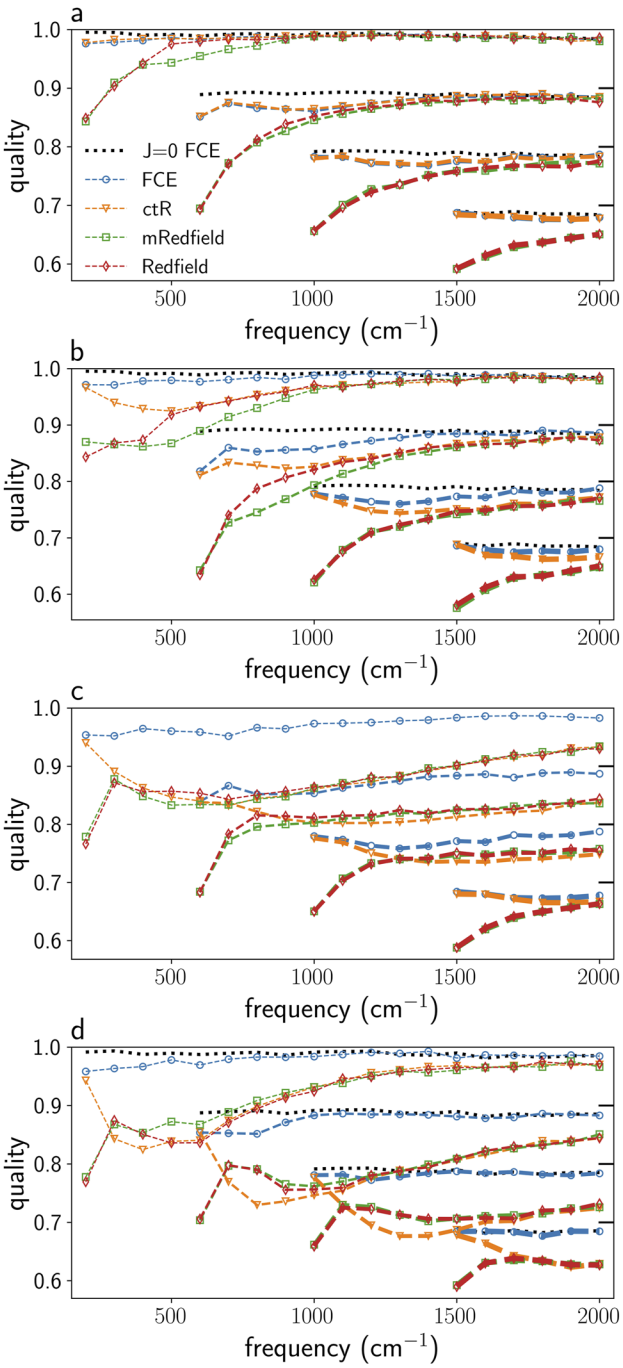

FIG. 4. Quality of absorption-type spectra at 300 K for excitonic coupling $J = 100$, 300, 500, and 750 cm^{-1} as a function of the excitonic energy gap. Qualities are shown for the absorption dipole factors (a) $f_{0,1}^{1,0}$ and (b) $f_{1,1}^{1,1}$, (c) CD dipole factor $f_{1,0}^{0,1}$, and (d) LD dipole factor $f_{-1,0}^{1,-1}$. A disorder of $\sigma_{\mathrm{FWHM}} = 140\ \mathrm{cm}^{-1}$ was used for the calculation of spectra. Note that the smallest possible exciton gap equals $2J$. For clarity, an offset in quality of 0.1, 0.2, and 0.3 was used for $J = 300$, 500, and 750 cm^{-1}, respectively. The quality of FCE spectra for the case $J = 0$ is shown as black dotted lines and act as a reference. Since CD spectra are zero when $J = 0$, FCE qualities are not shown for this case in panel (c).

The dotted black lines in Fig. 4 indicate the quality of FCE spectra for the case of zero coupling—which should correspond perfectly with the (exact) PI spectrum. The slight deviation from $Q = 1$ at large exciton gaps is due to an erroneous blue-shift and dampening of the high-energy absorption peak of the PI spectra (not shown). The PI calculations for Fig. 4 were performed by setting the average of the two site energies to zero in a given calculation and correcting for the energy shift afterward. When using the Hamiltonian in Eq. (34) without this correction, the PI spectra differed by as much as 10% from the exact (FCE, $J = 0$) spectra for large exciton gaps. We confirmed that this deviation is not due to incomplete convergence of the Monte Carlo integration (not shown), but is likely due to the inability of the second-order weak scheme (Appendix B) to handle the fast oscillations in the absorption tensor for large exciton gaps. The PI method, as presented in Sec. III, may therefore be inexact, and its accuracy must be tested for other systems and parameter ranges.

The FCE method performs well for all the strong couplings considered in Fig. 4. Only for the lowest exciton gap of $J = 300$ cm^{-1} is the quality somewhat worse than 95% [Fig. 4(b)]. For all the approximate methods, the linear spectra tend to the exact spectra with increasing excitonic gap, because the excitons become more localized and therefore increasingly resemble the localized states of the case $J = 0$. Another reason for the improvement in quality with excitonic energy gap (applicable to all dipole factors, including that of CD) is the diminishing contribution from the spectral density discussed below.

As discussed in Sec. IV A, the FCE method is inexact due to the contribution of excitonic propagators to the absorption tensor. For a given exciton gap, the excitation delocalization scales with the coupling strength, and the pigment participation factors $\gamma_{\alpha\beta\beta\alpha}$ and $\gamma_{\alpha\beta\beta\beta}$ (with $\alpha \neq \beta$) therefore increase with coupling (see Fig. S1). Since these factors are the coefficients of terms in Eq. (21) that contain excitonic propagators, the FCE method becomes less accurate as the excitonic coupling increases (when considering the same exciton gaps). In this work, vibrational modes of energy larger than 425 cm^{-1} were omitted, and the spectral density, therefore, decays after this frequency. Due to this decay, the exciton transfer rates (see Fig. S2) also decrease, and with them the contribution from terms containing propagators. For this reason, the FCE qualities in Fig. 4 may improve with coupling for a given amount of delocalization [quantified by $\gamma_{\alpha\beta\beta\alpha}$ in Eq. (22)] when the coupling is very large ($J \geq 300$ cm^{-1}). The other approximate methods show the same trend.

Compared to the variance in qualities for other methods, the independence of FCE qualities allows this method to be used for the calculation of absorption-type spectra with an almost constant, predictable error (especially for the molecular parameters in plant light-harvesting complexes).

For absorption-type spectra, the FCE method is equivalent to the time-convolutionless (TCL2) quantum master equation.[18] In agreement with our results, Fetherholf and Berkelbach[36] found the latter method to be accurate for the calculation of absorption spectra in a system with $\epsilon = 100$ cm^{-1} and $J = 100$ cm^{-1}. Strong coupling to bath modes is outside the scope of this article, but the above-mentioned authors found the TCL2 method (and therefore FCE) to be accurate for Ohmic–Lorentz spectral densities with reorganization energies as high as 150 cm^{-1}, a range that includes the value of 40 cm^{-1} used for the low-frequency mode in this study.

Due to the near absence of nonsecular effects (*vide supra*), the ctR spectra correspond very well with FCE spectra for the smallest exciton gap and for the dipole factor $f^{1,0}_{0,1}$, but ctR and FCE qualities may differ significantly for other dipole factors in Figs. 3 and 4—especially for the CD dipole factor and the LD dipole factor $f^{1,-1}_{-1,0}$ in panels (c) and (d). Due to the diminishing contribution from nonsecular contributions, which contain excitonic propagators, with excitonic energy gap, the difference in quality between FCE and ctR spectra decreases with coupling (for a given amount of delocalization).

The CD spectra are produced by dynamics of the electronic coherence between the ground state and *delocalized* excited states. The more delocalized the excitons, the smaller the relative contribution of nonsecular dynamics to the CD spectrum, and the more accurately the spectrum can be calculated with a secular method. For this reason, the ctR CD spectra in Figs. 3(c) and 4(c) have a higher quality for small energy gaps or for strong coupling, in which case the excitons are more delocalized, than for large gaps or moderate coupling.

As discussed in Sec. IV A, the electronic transition on the second pigment is LD-forbidden for the dipole factor $f^{1,-1}_{-1,0}$, and excitons that are predominantly localized on this pigment contribute to the LD spectrum mainly via transfer from other excitons. When excitons are fully delocalized, such transfer occurs due to population relaxation, as can be seen by comparing the coefficients for population transfer $\gamma_{\alpha\beta\beta\alpha}$ and nonsecular transfer $\gamma_{\alpha\beta\beta\beta}$ in Fig. S1 for small site energy gaps. The ratio of $\gamma_{\alpha\beta\beta\beta}$ and $\gamma_{\alpha\beta\beta\alpha}$ increases with energy gap, however, such that nonsecular transfer becomes important for correctly describing the LD spectrum at large excitonic energy gaps (until the spectra improve due to localization and decay of the spectral density). Although nonsecular transfer causes differences in quality between the ctR and FCE CD spectra, the excitation *delocalization* is more important for determining the quality of CD spectra.

Dinh and Renger[37] used perturbation theory to derive first-order non-secular and non-Markovian corrections $\alpha^{(1)}$ to the Partial Ordering Prescription (POP, see Sec. II C 3) for absorption and CD spectra. From an application of these corrections to the POP-spectra of the water-soluble chlorophyll-binding protein (WSCP), they found the non-secular and non-Markovian corrections to be small (on the order of a few percent of the overall signal). They also found these corrections to act by transferring oscillator strength from the strong to the weak excitonic transitions for absorption spectra, and by dampening the rotational strength of all transitions for CD spectra. In Fig. S10, we show the absorption spectrum for the dipole factor $f^{1,1}_{1,1}$ with $J = 100$ cm^{-1} and $\epsilon = 300$ cm^{-1} (the same site energy gap and coupling used in Fig. 5 of Ref. 37). In contrast to their results, the non-Markovian and non-secular methods (PI and FCE) produced absorption spectra in which the weaker transition has a smaller oscillator strength than in the secular or Markovian spectra. We also found the FCE CD spectra (not shown) to have slightly stronger rotational strength for all transitions compared to the secular or Markovian spectra. The source of the discrepancy between our results and their predictions would be found through a careful theoretical investigation, which is beyond the scope of this work. Notice, however, that the time-independent POP spectra in Fig. 3 may differ by almost 25% from the FCE spectra. The assumption made in Ref. 37 that the corrections are to be

small and perturbation theory valid, may therefore not hold for the spectral density considered in our work—especially given the large erroneous spectral shifts seen in the time-independent POP-spectra as discussed above.

The quality of FCE spectra is shown in Fig. S13 as a function of the excitonic energy gap for the case of equal site energies (i.e., J was varied with $\epsilon = 0$). The quality worsens (by about 5% for $f^{1,0}_{0,1}$) with excitonic energy gap up to about 470 cm^{-1} and thereafter improves at approximately the same rate as it worsened. Since excitons are maximally delocalized for such a system, the improvement of quality due to localization at large excitonic energy gaps is precluded, and the observed improvement is due to the diminishing contributions from the spectral density. From the initial worsening of quality—while the spectral density was large—we conclude that the quality of FCE (and by extension the other techniques) may worsen as more modes are considered in the spectral density.

C. Dependence of spectral quality on the dipole factor

In Secs. IV A and IV B, qualities and spectra were shown for four dipole factor matrices. In this section, we determine the dependence of the quality of absorption-type spectra on a generalized dipole factor.

To calculate the quality of approximate spectra, we normalized the spectra to their absolute maxima. Only the ratios of the dipole factor matrix elements in Eq. (13) are therefore important. Figures 5(a) and 5(b) show the quality of absorption-type spectra for $J = 15$ and 100 cm^{-1}, respectively, at 300 K as a function of the off-diagonal and diagonal element of the (bottom-right normalized) dipole factor matrix

$$f^{f_{11},f_{12}}_{f_{12},1} = \begin{bmatrix} f_{11} & f_{12} \\ f_{12} & 1 \end{bmatrix}. \tag{43}$$

This normalization can only be performed when the bottom right element of the dipole factor matrix is nonzero. For this reason, the dipole factor for CD, $f^{0,1}_{1,0}$, and the dipole factor for LD—with the dipole moment of the second pigment at the magic angle relative to the LD axis—$f^{1,-1}_{-1,0}$, are both mapped to $f_{12} \to \pm\infty$.

The assessments of the accuracy for the different methods made in Secs. IV A and IV B are evident in Fig. 5. The quality of FCE spectra is high for all dipole factors but is best when the magnitude of the diagonal element of the dipole factor is large compared to that of the off-diagonal elements. For moderate coupling [Fig. 5(a)], the quality of ctR spectra is also high for dipole factors in the same ranges, but it is significantly worse than the quality of FCE spectra when the magnitudes of the off-diagonal elements of the dipole factor are large. For strong coupling, dipole factors with large off-diagonal magnitudes produce more accurate ctR spectra than they do for moderate coupling. The reasons for the last two observations were discussed in Sec. IV B for CD spectra, for which the off-diagonal elements are infinitely large compared to the diagonal elements. The ctR method performs as good as FCE for the dipole factor $f^{1,0}_{0,1}$, but its accuracy (and hence the accuracy of the secular approximation) for other dipole factors depends on the coupling strength. For moderate coupling, nonsecular transfer is weaker than for strong coupling, and the secular approximation is valid for a broader range of off-diagonal dipole factor elements. When the coupling is strong, the spectral quality for some LD dipole factors is worse than for CD dipole factors, and the quality depends nontrivially on the dipole factor. The accuracy of the secular approximation, as a function of the dipole factor, can be modeled straightforwardly by considering the transformation of a time-independent matrix that summarizes the absorption tensor. Such a model is shown in Fig. S7 for the exciton gaps 101 cm^{-1} ($J = 15$ cm^{-1}) and 297 cm^{-1} ($J = 100$ cm^{-1}) and corresponds well with the ctR qualities in Fig. 5. Notice that the FCE qualities show a similar dependence on the dipole factor as ctR (albeit with less sensitivity) and as the expected accuracy of the secular approximation (Fig. S7). This dependence is explained by noting that the diagonal elements of the exciton-basis absorption tensor contains terms for which the second-order cumulant expansion is exact [Eq. (24)] together with inexact terms that contain excitonic propagators [Eq. (25)], whereas the off-diagonal elements only contain terms with propagators. For spectra with strong relative contribution from the diagonal tensor elements (i.e., spectra for which the secular approximation performs well), the relative contribution of the terms with excitonic propagators is smallest, and the FCE method, therefore, performs the best.

The quality of Redfield and modified Redfield spectra depends similarly on the dipole factor as the ctR spectra for the exciton energy gaps shown in Fig. 5, but these techniques perform worse than ctR for all dipole factors.

At the smallest possible excitonic energy gap (30 cm^{-1} for $J = 15$ cm^{-1} and 200 cm^{-1} for $J = 100$ cm^{-1}), the quality of absorption-type spectra is nearly zero for the dipole factor $(f_{11}, f_{12}) = (-1, 0)$. For this dipole factor, the LD spectrum is close to zero and the error in the stochastic integration is large—and the quality factor is therefore meaningless. Note that many of the LD dipole factors of CP29 correspond with $(f_{11}, f_{12}) = (-1, 0)$ and therefore may contribute little to the total LD spectrum.

At the energy gap of 101 cm^{-1} for $J = 15$ cm^{-1} and the dipole factor characterized by $(f_{11}, f_{12}) = (-1, 3)$, the FCE and PI spectra contain clear vibronic contributions (as shown in Fig. S8), which are absent in the results of the secular methods. Due to the strong vibronic contribution, the FCE and PI spectra agree qualitatively well with each other but differ significantly from the other spectra, which is the cause for the poor quality produced by the ctR, Redfield, and modified Redfield methods.

For moderate coupling, almost all of the absorption and LD dipole factors of the light-harvesting complex CP29 lie in the domain for which the FCE and ctR methods are accurate (as determined for the dimer considered in this study). As discussed above, the CD spectra deviate significantly from the exact spectra. Note, however, that contribution from the intrinsic CD strength of pigment molecules[38] may cause significant differences between experimental spectra and exact spectra calculated from the excitonic contribution alone. For this reason, the use of accurate methods for the calculation of CD spectra may not be worth their cost. For strong coupling, LD contributions from many of the pigment pairs in CP29 may be considerably impacted by the poor performance of the secular methods. Given the similar dipole strengths of the chlorophyll pigments in other light-harvesting complexes, and the fact that the dipole vectors in CP29 do not have a particular ordered arrangement, the secular LD spectra of light-harvesting complexes that contain

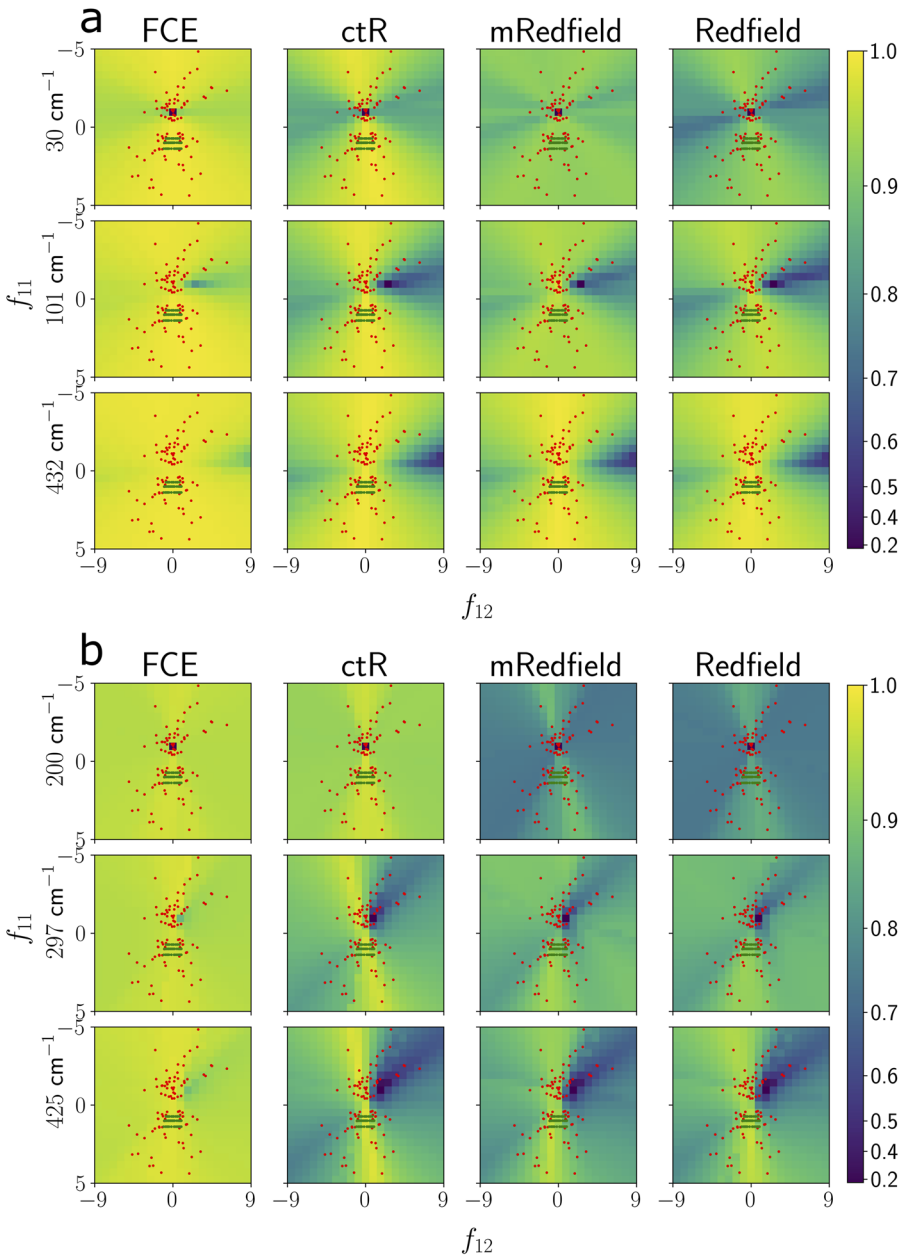

FIG. 5. Quality of absorption-type spectra at 300 K as a function of the dipole factor $f^{f_{11},f_{12}}_{f_{12},1}$ at the excitation energy gaps indicated for (a) $J = 15$ cm^{-1} and (b) $J = 100$ cm^{-1}. The other parameters are the same as for the calculations for Fig. 3. The dipole factors for LD and OD spectra of CP29 are indicated by red and green dots, respectively, and were calculated from the PDB structure 5xnl.pdb using a dipole strength of 13.96 D^2 for Chl *a* as in Ref. 26.

strongly coupled pigments may, in general, correspond poorly to exact spectra.

In photosynthetic light-harvesting complexes, the average delocalization length varies from slightly more than one pigment for the PCE545 complex of cryptophytes[39] to seven or eight pigments in the circularly symmetrical bacterial complexes LH1 and LH2[40] and the chlorosome antenna of green sulfur bacteria.[41] The delocalization length in CP29 is estimated to be two to four pigments.[29] The qualities at the smallest and largest energy gaps in either Figs. 5(a) or 5(b) represent the cases for delocalized and predominantly localized excitons in a dimer, respectively. Based on the similarity between the dependence of these qualities on the dipole factor for FCE, we conclude that the results of this study will likely extend to aggregates with multiple pigments and that the FCE method may therefore be applied to calculate accurate absorption-type spectra of aggregates with multiple pigments, irrespective of the coupling between pigments. The same reasoning may be applied to the ctR method, and absorption and LD spectra may therefore likely be calculated qualitatively accurately with the ctR method when all the pigments in a pigment aggregate are moderately coupled (i.e., with couplings on the order of 15 cm^{-1}). For strong coupling, the spectral quality of ctR differs significantly in its dependence on the

dipole factor for localized and delocalized excitons, and extension of results in this study to the case for multiple pigments is not straightforward. Based on the dependence of accuracy on the dipole factor for intermediate delocalized states (297 cm^{-1}), however, LD spectra for partially localized states in multipigment aggregates may have poor quality.

V. CONCLUSION

In this study, we assessed the accuracy of approximate linear absorption-type spectra calculated with the FCE, ctR, Redfield, and modified Redfield methods. We used a pigment dimer as a model system and considered a realistic model spectral density for photosynthetic light-harvesting complexes in plants. We included inhomogeneous disorder and calculated the accuracy of spectra at 300 and 100 K. Among the approximate methods considered in this study, FCE performs best for the calculation of all types of linear spectra for all molecular parameters and at all temperatures. This method is most accurate for absorption spectra and least accurate for CD spectra. However, for the latter, it is still about 95% accurate. The ctR method performs well for the calculation of absorption and LD spectra when the interpigment coupling is moderately large (~15 cm^{-1}) but performs poorly for the calculation of CD spectra for moderate coupling. Spectra calculated with the ctR method are generally of much lower quality when strong interpigment coupling is present, but absorption spectra are still at least 93% accurate (for the parameters in this study). When strong coupling is present, ctR LD spectra may be of lower quality than CD spectra, and the spectra calculated with both of these techniques may differ more than 15% from the exact spectra. The Redfield and modified Redfield methods perform worse than the ctR method under nearly all circumstances and most notably when the coupling between pigment molecules is strong or the difference between site energies is small, and should not be used if a more accurate method is available. Non-Markovianity is very important for the accuracy of methods, and augmenting the Redfield rates with imaginary, but time-independent and Markovian, contributions generally degrades its performance. For the weak system–bath coupling in the light-harvesting complexes of plants, the quality of approximate spectra is not sensitive to resonance of the exciton gap with intramolecular modes when inhomogeneous disorder is included realistically, and the spectral accuracy is nearly independent of the temperature.

Future work may focus on quantitatively extending the results in this study to pigment aggregates with more than two pigment molecules, especially when strong interpigment coupling is present and on determining the dependence of spectral quality for fluorescence spectra calculated with these methods.

SUPPLEMENTARY MATERIAL

See the supplementary material for additional figures.

ACKNOWLEDGMENTS

We acknowledge the University of Pretoria Physics Department's SuperMicro Power-SERVER. J.A.N. acknowledges financial support from the South African National Research Foundation (Grant No. 101404) and South African Quantum Technology Initiative (Grant No. SAQuTI03/2021). T.P.J.K. acknowledges funding from the National Laser Centre Rental Pool Program (Grant No. LRERA13). T.M. thanks the Czech Science Foundation (GAČR) (Grant No. 22-26376S) for financial support.

AUTHOR DECLARATIONS

Conflict of Interest

The authors have no conflicts to disclose.

Author Contributions

J. A. Nöthling: Conceptualization (equal); Formal analysis (lead); Investigation (lead); Methodology (lead); Software (lead); Visualization (lead); Writing – original draft (lead); Writing – review & editing (supporting). **Tomáš Mančal**: Conceptualization (supporting); Formal analysis (supporting); Funding acquisition (supporting); Supervision (supporting); Writing – review & editing (equal). **T. P. J. Krüger**: Conceptualization (equal); Funding acquisition (lead); Investigation (supporting); Methodology (supporting); Project administration (lead); Resources (lead); Supervision (lead); Writing – review & editing (equal).

DATA AVAILABILITY

The data that support the findings of this study are available from the corresponding author upon reasonable request.

APPENDIX A: DIPOLE FACTOR FOR LINEAR DICHROISM OF DISK-SHAPED COMPLEXES

An LD spectrum is the difference between absorption spectra measured for two light beams with mutually perpendicular polarization vectors. For a beam propagating in the (Cartesian) $\hat{\boldsymbol{y}}$ direction, the LD spectrum is

$$\mathrm{I}^{\mathrm{LD}}(\omega) = \mathrm{I}_z^{\mathrm{A}}(\omega) - \mathrm{I}_x^{\mathrm{A}}(\omega), \tag{A1}$$

where x and z indicates the polarization of the light used to illuminate the sample. LD spectra of small molecules are often measured by means of gel compression. For this technique, complexes are dissolved in a polyacrylamide solvent, which forms a gel.[42] The gel is then compressed along the $\hat{\boldsymbol{x}}$ and $\hat{\boldsymbol{y}}$ dimensions by a factor $k \in (0, 1)$ and allowed to expand along the $\hat{\boldsymbol{z}}$ dimension. The LD spectrum [Eq. (A1)] is measured in the compressed state.

To derive the dipole factor $f_{mn}^{\mu,\mathrm{LD}}$ in Eq. (15), we perform the following mental experiment. We consider a small macroscopic volume V of the uncompressed gel containing many disk-shaped complexes, each with N pigments. The complexes are randomly oriented and therefore produce no LD signal. Without changing their orientations, we take all the complexes in V and arrange them on the surface of a sphere that fits within V, such that the normal vectors to the disks (which we assume can be assigned unambiguously) point radially outward. Since we measure the far-field LD spectrum,

no signal is produced from this arrangement. We then compress the gel. The complexes now lie on the surface of an ellipsoid of which we can determine the geometry from the compression factor k. For this arrangement, the LD signal is nonzero. We now place the complexes at their original positions on the surface of the sphere, again without changing their orientations. While the complexes are spaced uniformly on the surface of the sphere, their normal vectors do not point radially outward. Instead, in spherical coordinates, the zenith angle β for the normal vectors can be expressed in terms of the zenith angle ϕ of their position vectors (which do point radially outward) as

$$\beta = \frac{\pi}{2} - \tan^{-1}\left(k \tan\left(\frac{\pi}{2} - \phi\right)\right). \tag{A2}$$

Now consider the dipole moment of pigment m, $\boldsymbol{\mu}_m$ that makes an angle α with the normal vector of its disk. Since the molecules were randomly oriented originally, the many dipoles $\boldsymbol{\mu}_m$ at any coarse-grained position on the spherical surface, populate a cone. For the complexes on the pole ($\phi = \beta = 0$), the dipole cone is parameterized as

$$\begin{bmatrix} \mu_{m,x} \\ \mu_{m,y} \\ \mu_{m,z} \end{bmatrix} = |\boldsymbol{\mu}_m| \begin{bmatrix} \sin\alpha\cos t \\ \sin\alpha\sin t \\ \cos\alpha \end{bmatrix}, \quad t \in (0, 2\pi). \tag{A3}$$

In general, for a disk normal vector pointing in the spherical angular direction (β, γ), the parameterized dipole cone is determined from Eq. (A3) by consecutive Euler rotations as

$$\begin{bmatrix} \mu_{m,x} \\ \mu_{m,y} \\ \mu_{m,z} \end{bmatrix} = |\boldsymbol{\mu}_m| \begin{bmatrix} \cos\gamma(\cos\beta\sin\alpha\cos t + \sin\beta\cos\alpha) - \sin\gamma\sin\alpha\sin t \\ \sin\gamma(\cos\beta\sin\alpha\cos t + \sin\beta\cos\alpha) + \cos\gamma\sin\alpha\sin t \\ -\sin\beta\sin\alpha\cos t + \cos\beta\cos\alpha \end{bmatrix}. \tag{A4}$$

We can now calculate the LD dipole factor by performing a surface integral over the surface of the sphere (over which the complexes are uniformly distributed). We also integrate over the coordinate t that parameterizes the dipole cone around the disk normal,

$$f_{mn}^{\mu,\mathrm{LD}} = \int_0^{2\pi} dt \int_0^{2\pi} d\gamma \int_0^{\pi} d\phi \left[\mu_{m,z}\mu_{n,z} - \mu_{m,x}\mu_{n,x}\right] \sin\phi. \tag{A5}$$

By using the parameterization of Eq. (A4) and a result from Eq. (A2),

$$\cos\beta = \frac{k\cot\phi}{\sqrt{k^2\cot^2\phi + 1}}, \tag{A6}$$

we obtain (after some algebra and online integral calculation)

$$f_{mn}^{\mu,\mathrm{LD}} = \pi^2 L_k \left(\boldsymbol{\mu}_m \cdot \boldsymbol{\mu}_n - 3|\boldsymbol{\mu}_m||\boldsymbol{\mu}_n| \cos\alpha_m \cos\alpha_n\right) \tag{A7}$$

with

$$\begin{aligned} L_k &= \int_0^{\pi} d\phi \left(1 - 3\cos^2\beta\right) \sin\phi \\ &= -4 - \frac{3(1-u^2)\ln\left(\frac{1+u}{1-u}\right) - 6u}{u^3}, \end{aligned} \tag{A8}$$

where $u = \sqrt{1-k^2}$. In general, one is interested only in the relative intensity of the LD spectrum, and we simply define

$$f_{mn}^{\mu,\mathrm{LD}} = \boldsymbol{\mu}_m \cdot \boldsymbol{\mu}_n - 3|\boldsymbol{\mu}_m||\boldsymbol{\mu}_n| \cos\alpha_m \cos\alpha_n. \tag{A9}$$

APPENDIX B: SECOND-ORDER WEAK SCHEME

The explicit order 2 weak scheme that we use to propagate the stochastic matrices can be derived by a straightforward but somewhat tedious calculation from the vector expressions in Chap. 15 of Kloeden and Platen,[31]

$$\rho_i = \left[I + \frac{1}{2}\Delta - (\Delta H + \Delta\Xi_{i-1}) \cdot \left(iI + \frac{1}{2}\Delta H + \frac{1}{2}\Delta\Xi_{i-1}\right)\right]\rho_{i-1}, \tag{B1}$$

where, for a given discretization, I is the identity matrix, $\Delta = \delta t I$, and Ξ_{i-1} is a diagonal matrix with $\xi_{n,i-1}$ on the nth diagonal position. In Eq. (B1), $(\cdot)$ denotes matrix multiplication.

REFERENCES

[1] G. Garab and H. van Amerongen, "Linear dichroism and circular dichroism in photosynthesis research," Photosynth. Res. **101**, 135–146 (2009).
[2] A. Rodger and B. Nordén, *Circular Dichroism and Linear Dichroism*, Oxford Classical Monographs (Oxford University Press, 1997).
[3] E. Romero, M. Mozzo, I. H. M. van Stokkum, J. P. Dekker, R. van Grondelle, and R. Croce, "The origin of the low-energy form of photosystem I light-harvesting complex Lhca4: Mixing of the lowest exciton with a charge-transfer state," Biophys. J. **96**, L35–L37 (2009).
[4] B. Brüggemann, K. Sznee, V. Novoderezhkin, R. van Grondelle, and V. May, "From structure to dynamics: Modeling exciton dynamics in the photosynthetic antenna PS1," J. Phys. Chem. B **108**, 13536–13546 (2004).
[5] T. P. J. Krüger, V. I. Novoderezhkin, C. Ilioaia, and R. van Grondelle, "Fluorescence spectral dynamics of single LHCII trimers," Biophys. J. **98**, 3093–3101 (2010).
[6] V. I. Novoderezhkin, M. A. Palacios, H. van Amerongen, and R. van Grondelle, "Energy-transfer dynamics in the LHCII complex of higher plants: Modified Redfield approach," J. Phys. Chem. B **108**, 10363–10375 (2004).

[7]C. Ramanan, J. M. Gruber, P. Malý, M. Negretti, V. Novoderezhkin, T. P. J. Krüger, T. Mančal, R. Croce, and R. van Grondelle, "The role of exciton delocalization in the major photosynthetic light-harvesting antenna of plants," Biophys. J. **108**, 1047–1056 (2015).
[8]M. A. Palacios, F. L. de Weerd, J. A. Ihalainen, R. van Grondelle, and H. van Amerongen, "Superradiance and exciton (de)localization in light-harvesting complex II from green plants?," J. Phys. Chem. B **106**, 5782–5787 (2002).
[9]B. M. Bulheller, A. Rodger, and J. D. Hirst, "Circular and linear dichroism of proteins," Phys. Chem. Chem. Phys. **9**, 2020–2035 (2007).
[10]R. Croce, T. Morosinotto, S. Castelletti, J. Breton, and R. Bassi, "The Lhca antenna complexes of higher plants Photosystem I," Biochim. Biophys. Acta, Bioenerg. **1556**, 29–40 (2002).
[11]Y. Tanimura and R. Kubo, "Time evolution of a quantum system in contact with a nearly Gaussian-Markoffian noise bath," J. Phys. Soc. Jpn. **58**, 101–114 (1989).
[12]A. Ishizaki and G. R. Fleming, "Theoretical examination of quantum coherence in a photosynthetic system at physiological temperature," Proc. Natl. Acad. Sci. U. S. A. **106**, 17255–17260 (2009).
[13]C. Kreisbeck, T. Kramer, and A. Aspuru-Guzik, "Scalable high-performance algorithm for the simulation of exciton dynamics. Application to the light-harvesting complex II in the presence of resonant vibrational modes," J. Chem. Theory Comput. **10**, 4045–4054 (2014).
[14]V. I. Novoderezhkin, E. Romero, and R. van Grondelle, "How exciton-vibrational coherences control charge separation in the photosystem II reaction center," Phys. Chem. Chem. Phys. **17**, 30828–30841 (2015).
[15]J. M. Moix, J. Ma, and J. Cao, "Förster resonance energy transfer, absorption and emission spectra in multichromophoric systems. III. Exact stochastic path integral evaluation," J. Chem. Phys. **142**, 094108 (2015); arXiv:1501.05679.
[16]T. Renger and R. A. Marcus, "On the relation of protein dynamics and exciton relaxation in pigment-protein complexes: An estimation of the spectral density and a theory for the calculation of optical spectra," J. Chem. Phys. **116**, 9997–10019 (2002).
[17]L. Valkunas, D. Abramavicius, and T. Mančal, *Molecular Excitation Dynamics and Relaxation* (Wiley-VCH Verlag GmbH & Co. KGaA, Weinheim, Germany, 2013).
[18]J. Ma and J. Cao, "Förster resonance energy transfer, absorption and emission spectra in multichromophoric systems. I. Full cumulant expansions and system-bath entanglement," J. Chem. Phys. **142**, 094106 (2015); arXiv:1501.05679.
[19]A. Gelzinis, D. Abramavicius, and L. Valkunas, "Absorption lineshapes of molecular aggregates revisited," J. Chem. Phys. **142**, 154107 (2015).
[20]M. Jassas, J. Chen, A. Khmelnitskiy, A. P. Casazza, S. Santabarbara, and R. Jankowiak, "Structure-based exciton Hamiltonian and dynamics for the reconstituted wild-type CP29 protein antenna complex of the photosystem II," J. Phys. Chem. B **122**, 4611–4624 (2018).
[21]L. Cupellini, F. Lipparini, and J. Cao, "Absorption and circular dichroism spectra of molecular aggregates with the full cumulant expansion," J. Phys. Chem. B **124**, 8610–8617 (2020).
[22]M. Schröder, U. Kleinekathöfer, and M. Schreiber, "Calculation of absorption spectra for light-harvesting systems using non-Markovian approaches as well as modified Redfield theory," J. Chem. Phys. **124**, 084903 (2006).
[23]S. Mukamel, *Principles of Nonlinear Optical Spectroscopy* (Oxford University Press, 1995).
[24]W. M. Zhang, T. Meier, V. Chernyak, and S. Mukamel, "Exciton-migration and three-pulse femtosecond optical spectroscopies of photosynthetic antenna complexes," J. Chem. Phys. **108**, 7763 (1998).
[25]J. Olšina, T. Kramer, C. Kreisbeck, and T. Mančal, "Exact stochastic unraveling of an optical coherence dynamics by cumulant expansion," J. Chem. Phys. **141**, 164109 (2014); arXiv:1309.0749.
[26]V. Mascoli, V. Novoderezhkin, N. Liguori, P. Xu, and R. Croce, "Design principles of solar light harvesting in plants: Functional architecture of the monomeric antenna CP29," Biochim. Biophys. Acta, Bioenerg. **1861**, 148156 (2020).
[27]E. J. G. Peterman, T. Pullerits, R. van Grondelle, and H. van Amerongen, "Electron-phonon coupling and vibronic fine structure of light-harvesting complex II of green plants: Temperature dependent absorption and high-resolution fluorescence spectroscopy," J. Phys. Chem. B **101**, 4448–4457 (1997).
[28]S. Jurinovich, L. Viani, I. G. Prandi, T. Renger, and B. Mennucci, "Towards an *ab initio* description of optical spectra of light-harvesting antennae: Application to the CP29 complex of photosystem II," Phys. Chem. Chem. Phys. **17**, 14405–14416 (2015).
[29]F. Müh, D. Lindorfer, M. Schmidt am Busch, and T. Renger, "Towards a structure-based exciton Hamiltonian for the CP29 antenna of photosystem II," Phys. Chem. Chem. Phys. **16**, 11848–11863 (2014).
[30]R. C. Jennings, G. Zucchelli, R. Croce, and F. M. Garlaschi, "The photochemical trapping rate from red spectral states in PSI-LHCI is determined by thermal activation of energy transfer to bulk chlorophylls," Biochim. Biophys. Acta, Bioenerg. **1557**, 91–98 (2003).
[31]P. E. Kloeden and E. Platen, *Numerical Solution of Stochastic Differential Equations*, Stochastic Modelling and Applied Probability (Springer Berlin Heidelberg, 2011).
[32]F. Fassioli, R. Dinshaw, P. C. Arpin, and G. D. Scholes, "Photosynthetic light harvesting: Excitons and coherence," J. R. Soc., Interface **11**, 20130901 (2014).
[33]S. J. Jang and B. Mennucci, "Delocalized excitons in natural light-harvesting complexes," Rev. Mod. Phys. **90**, 035003 (2018); arXiv:1804.09711.
[34]E. Collini, C. Y. Wong, K. E. Wilk, P. M. G. Curmi, P. Brumer, and G. D. Scholes, "Coherently wired light-harvesting in photosynthetic marine algae at ambient temperature," Nature **463**, 644–647 (2010).
[35]F. Segatta, L. Cupellini, S. Jurinovich, S. Mukamel, M. Dapor, S. Taioli, M. Garavelli, and B. Mennucci, "A quantum chemical interpretation of two-dimensional electronic spectroscopy of light-harvesting complexes," J. Am. Chem. Soc. **139**, 7558–7567 (2017).
[36]J. H. Fetherolf and T. C. Berkelbach, "Linear and nonlinear spectroscopy from quantum master equations," J. Chem. Phys. **147**, 244109 (2017); arXiv:1709.04075.
[37]T.-C. Dinh and T. Renger, "Towards an exact theory of linear absorbance and circular dichroism of pigment-protein complexes: Importance of non-secular contributions," J. Chem. Phys. **142**, 034104 (2015).
[38]D. Lindorfer, F. Müh, and T. Renger, "Origin of non-conservative circular dichroism of the CP29 antenna complex of photosystem II," Phys. Chem. Chem. Phys. **19**, 7524–7536 (2017).
[39]V. I. Novoderezhkin, A. B. Doust, C. Curutchet, G. D. Scholes, and R. van Grondelle, "Excitation dynamics in phycoerythrin 545: Modeling of steady-state spectra and transient absorption with modified Redfield theory," Biophys. J. **99**, 344–352 (2010).
[40]R. van Grondelle and V. I. Novoderezhkin, "Energy transfer in photosynthesis: Experimental insights and quantitative models," Phys. Chem. Chem. Phys. **8**, 793–807 (2006).
[41]S. Jun, C. Yang, S. Choi, M. Isaji, H. Tamiaki, H. Ihee, and J. Kim, "Exciton delocalization length in chlorosomes investigated by lineshape dynamics of two-dimensional electronic spectra," Phys. Chem. Chem. Phys. **23**, 24111–24117 (2021).
[42]G. Zucchelli, R. C. Jennings, F. M. Garlaschi, P. Dainese, J. Breton, and R. Bassi, "Gaussian decomposition of absorption and linear dichroism spectra of outer antenna complexes of photosystem II," Biochemistry **33**, 8982–8990 (1994).